Journal of Materials Research and Technology 43 (2026) 1646–1664

Contents lists available at ScienceDirect

Journal of Materials Research and Technology

journal homepage: www.elsevier.com/locate/jmrt

# Organic therapeutic component-modified carbonated apatite and biopolymer composites for next-generation implant coatings

Monika Furko [a,*], Zsolt Fogarassy [a], Marta Alves [b], Katalin Balázsi [a], Csaba Balázsi [a]

[a] Centre for Energy Research, HUN-REN, Konkoly-Thege rd. 29-33, Budapest, H-1121, Hungary
[b] Technical University of Lisbon, Department of Chemical Engineering (DEQ), Lisbon, Portugal

ARTICLE INFO

*Keywords:*
Bioceramics
Biopolymers
Composites
Biodegradability
Corrosion

ABSTRACT

The integration of bioactive ceramics with biopolymers represents a frontier in the development of advanced materials for tissue engineering. This study investigates the synthesis and characterization of novel organic therapeutic component-modified carbonated apatite (cAp) composites blended with biopolymers. Carbonated apatite was prepared using a wet chemical precipitation method. Subsequently, the cAp was functionally modified by incorporating therapeutic components: organic strontium ($Sr^{2+}$), magnesium ($Mg^{2+}$), and zinc ($Zn^{2+}$). The resulting functionalized cAp powder (fcAP) was then integrated into two distinct biopolymer matrices: polycaprolactone (PCL) and cellulose acetate (CA). The resulting composites were successfully deposited as non-continuous coatings or clusters onto a rough metallic implant surface. These layers exhibited a highly porous three-dimensional microstructure, which is beneficial for enhanced cell adhesion. Comprehensive physicochemical characterization, utilizing techniques including Scanning Electron Microscopy with Energy-Dispersive X-ray Spectroscopy (SEM-EDX), Transmission Electron Microscopy (TEM), X-ray Diffraction (XRD), and Fourier-Transform Infrared Spectroscopy (FT-IR), confirmed that the synthesized calcium phosphate phase was carbonated apatite and verified the successful incorporation and presence of the therapeutic elements. Quantitative analysis of the therapeutic fcAp revealed a Ca to P molar ratio of 1.60, which closely approximates that of natural bone. The composite coatings significantly enhanced the corrosion resistance of the metallic substrate, achieving a 20-46% reduction in the corrosion rate compared to bare titanium. After one month of immersion testing, the two biopolymer composites exhibited distinct degradation behaviors: PCL-fcAp showed a slight weight loss of 0.5%, while the CA-fcAp demonstrated exceptional hydrolytic stability, presenting a minimal weight loss of less than 0.15%.

## 1. Introduction

Titanium-based alloys are the predominant materials for load-bearing orthopedic and dental implants, owing to their excellent mechanical strength, corrosion resistance, and biocompatibility [1]. Nevertheless, achieving rapid and stable osseointegration, defined as a direct structural and functional connection between living bone and the implant surface, remains a significant clinical challenge. The inherent biological inertia of titanium can result in inadequate early bone bonding, fibrous encapsulation, micro-motion, and eventual implant loosening or failure [2]. To address these limitations, surface engineering approaches aim to develop bioactive coatings that emulate the natural composition and architecture of bone, thereby improving cellular interactions and integration [3]. A particularly innovative strategy involves fabricating ultrathin composite coatings composed of nanocrystalline or amorphous apatite (nAp) embedded within biodegradable biopolymer matrices [4]. Carbonated hydroxyapatite (cAp), which closely resembles the primary inorganic phase of bone, offers high osteoconductivity and enhanced surface bioactivity [5]. Incorporating cAp into biopolymers such as polycaprolactone (PCL) or cellulose acetate (CA) produces a composite material that synergistically combines the bioactivity of ceramics with the adjustable degradation, mechanical flexibility, and drug-eluting potential of polymers [6–10]. PCL is a hydrophobic, semi-crystalline polyester recognized for its excellent biocompatibility, slow degradation profile (spanning years), ease of processing, and mechanical toughness, which provides durable structural support [11]. In contrast, cellulose acetate exhibits favorable biocompatibility, hydrophilicity, and film-forming properties, while

* Corresponding author.
*E-mail address:* furko.monika@ek.hun-ren.hu (M. Furko).

https://doi.org/10.1016/j.jmrt.2026.06.162
Received 29 January 2026; Received in revised form 13 May 2026; Accepted 16 June 2026
Available online 17 June 2026

also facilitating initial protein adsorption [12]. Its degradation rate is more tunable than that of PCL, typically ranging from months to several years depending on the degree of substitution and environmental conditions [13]. These polymeric matrices serve as carriers and modifiers for cAp, governing coating adhesion, degradation kinetics, and the release profiles of incorporated agents [14]. To further augment biological performance, the strategic inclusion of essential therapeutic trace elements in organic complex form presents an effective solution. Magnesium (Mg), strontium (Sr), and zinc (Zn) are critical co-factors in bone metabolism. Their organic complexes, such as Mg-pidolate, Sr-ranelate, and Zn-gluconate, can provide superior bioavailability and more controlled release compared to inorganic salts [15–18]. Magnesium pidolate supplies $Mg^{2+}$ ions, which are fundamental for osteoblast adhesion, proliferation, and the initial phases of bone matrix mineralization, with deficiency linked to impaired bone growth [19]. Pidolic acid, derived from glutamic acid in vivo, plays a role in cellular metabolism and energy production, and enhances the absorption and cellular uptake of magnesium [20]. Strontium ranelate, as a source of $Sr^{2+}$ ions, exhibits a unique dual action by promoting osteoblast-mediated bone formation while inhibiting osteoclast-mediated bone resorption [21]. The ranelate organic group is clinically established to increase bone mass and strength in osteoporotic patients [22]. Zinc gluconate contributes crucially to collagen synthesis and alkaline phosphatase activity, and possesses anti-inflammatory and antibacterial properties, with the gluconate component ensuring good solubility and bioavailability [23]. Beyond chemical composition, surface topography is equally critical. Coating roughness at the micro- and nanoscale profoundly influences cellular behavior [24]. An optimized, hierarchical rough surface increases surface area and presents physical cues that promote migration, adhesion, spreading, and cytoskeletal organization of bone-forming cells (such as osteoblasts, pre-osteoblasts, mesenchymal stem cells) [25]. Such a surface also enhances mechanical interlocking with newly formed bone and stimulates the osteogenic differentiation of progenitor cells, thereby accelerating bone formation and remodeling at the interface to strengthen osseointegration [26]. While continuous bioactive coatings have been extensively studied, they face challenges such as delamination from poor adhesion, constrained control over degradation, and the potential to act as a barrier to direct bone-implant contact [27,28]. An emerging approach to overcome these issues employs non-continuous or discrete coatings. This design creates a micro-structured surface where bioactive clusters are interspersed with exposed regions of the roughened implant substrate. This architecture offers several benefits: it permits direct osseointegration with the underlying titanium for robust mechanical fixation; it enables synchronized bone ingrowth into the inter-cluster voids as the biodegradable coating resorbs, avoiding a long-term barrier effect [29]; and it reduces interfacial stress concentrations, thereby lowering the risk of coating delamination [30]. Consequently, in this study, composite coatings were intentionally engineered to be non-continuous, synergistically combining material bioactivity with the topological advantages of a discrete surface pattern. A further novel aspect of this work is the integration of carbonated apatite with therapeutic organic complexes. Although the doping of hydroxyapatite with inorganic $Mg^{2+}$, $Sr^{2+}$, and $Zn^{2+}$ ions is well-established [31], the incorporation of their organic complexes (Mg-pidolate, Sr-ranelate, Zn-gluconate) into a carbonated apatite matrix represents, to our knowledge, a new approach. These organic ligands were selected not merely as carriers, but for their enhanced bioavailability and specific biological functions, aiming to achieve a more controlled and synergistic therapeutic release profile compared to inorganic salts. Additionally, this study provides a direct comparative analysis of two distinct polymer matrices, a synthetic, hydrophobic, slow-degrading polyester (PCL) and a natural, more hydrophilic derivative (CA), for the same therapeutic cAp composite. This comparison provides practical insights into tailoring coating properties to specific clinical requirements, such as long-term mechanical support versus shorter-term bioactivity. Collectively, this integrated approach holds considerable promise for improving the early fixation, long-term stability, and overall success of load-bearing titanium implants in demanding clinical applications.

## 2. Materials and methods

### 2.1. Powder synthesis: preparation of nanocrystalline carbonated apatite (cAp) and therapeutic component added carbonated apatite (fcAP) powders

Suspensions intended for the wet precipitation of carbonated apatite (cAp) were prepared by dissolving calcium gluconate ($HOH_2C(CH(OH))_4COOCa$, Acros Organics, 99%) in double-distilled water in 3g/100 mL concentration. Subsequently, 10 mL of 0.06 g/L disodium hydrogen phosphate ($Na_2HPO_4$, VWR International Ltd. - 99%, AnalaR NORMAPUR) solution was gradually dripped into the solution with vigorous agitation (1400 rpm) at room temperature, thereby adjusting the calcium-to-phosphorus molar ratio to 5:3. The addition of the phosphorus precursor immediately caused white powder precipitation. The pH of the suspensions was adjusted to 11 by gradually adding a suitable amount (0.6 g/L) of anhydrous sodium carbonate ($Na_2CO_3$ anhydrous, (VWR International Ltd. - ≥99.5% ACS), and the suspension was left for 24 h to obtain phase transformation and carbonated apatite particles.

To prepare the functionalized carbonated apatite (fcAp) powder, cAp powder was combined with magnesium L-pidolate ($C_{10}H_{12}MgN_2O_6$, VWR International Ltd., ≥98%, high purity), zinc gluconate ($HOH_2C(CH(OH))_4COOZn$, VWR International Ltd. - ≥99.0%, AnalaR NORMAPUR), and strontium ranelate ($C_{12}H_6N_2O_8SSr_2$,VWR International Ltd. - ≥99.0%, AnalaR NORMAPUR) in a weight proportion of 3:1:1:1, (3g cAp, 1g magnesium L-pidolate, 1 g zinc gluconate and 1 g strontium ranelate) using ethanol as a dispersant. These weight ratios were specifically chosen to achieve a high concentration of therapeutic elements, all while maintaining the composite coating's workability and structural stability. The mixture was stirred intensely for 2 h at room temperature and 1400 rpm to ensure a uniform dispersion, after which it was permitted to settle. After sedimentation, the solid phase was rinsed repeatedly with ethanol to remove residual reagents and then dried at 100 °C for 4 h. The collected dried powder was then ready for further characterization and use in the spin coating process.

### 2.2. Preparation of composite thin layers by spin coating

Titanium disks (diameter: 30 mm; thickness: 3 mm) were used as substrates (donated by Sanatmetal Kft, Eger, Hungary). The surface of all titanium alloy discs was roughened by titanium plasma spraying (TPS: Titanium Plasma Spray ISO 5832-2 ASTM F1580, layer thickness 0.25 mm). The thickness of the titanium primer coating is 250 ± 50 μm, and the grain size of unalloyed titanium is 180 μm (ISO 5832-2). Polycaprolactone (PCL, average $M_w$ ~80,000, Sigma-Aldrich) and cellulose acetate (CA, average $M_w$ ~ 100,000, Acros Organics, Geel, Antwerp, Belgium, acetyl content 39.8%)) were used as biopolymers and bioadhesives. Using a Chemat Technology Spin Coater KW-4A, biopolymer and composite coatings were applied to metallic implant surfaces through a spin-coating method. CA polymer was solubilized in acetone (VWR International Ltd., ≥99%, technical), 2 g CA in 20 mL acetone (10% w/v), and PCL in dichloromethane (DCM, ACS reagent, ≥99.5%, Merck KGaA, Darmstadt, Germany)) 2 g PCL in 20 mL acetone (10% w/v). For the fcAP-PCL composite thin layer, fcAP particles and PCL were combined in DCM at a 1:2 wt ratio (1g fcAp powder and 2 g PCL powder were dispersed in DCM) and thoroughly stirred to achieve good homogeneity. Similarly, the fcAP-CA composite was produced by dispersing fcAP particles in acetone with CA polymer, also at a 1:2 wt ratio (1g fcAp powder and 2 g CA powder were dispersed in acetone thoroughly). The implant surfaces were coated with these mixtures at a volume of 200 μL per surface area and subjected to a two-stage spin-coating process: an

initial stage at 500 rpm for uniform suspension spreading, and a subsequent stage at 2000 rpm to aid in the evaporation of the solvent at ambient temperature.

### 2.3. Morphological characterization methods

The morphological assessments of cAp and fcAp powders as well as the CA and PCL polymers, and both composite layer types were performed using a scanning electron microscope (SEM, Thermo Scientific Scios2, Waltham, MA, USA) with an Energy Dispersive X-ray Spectrometry system (Oxford Instruments EDS detector X-Maxn, Abingdon, UK). Map-sum spectra were recorded at an accelerating voltage of 16 keV. For cross-sectional analyses, FIB measurements were done with LEO 1540XB Crossbeam workstation. The ion beam parameters in FIB milling mode were 30 kV accelerating voltage and 5 nA beam current. For SEM/FIB measurements, the samples were tilted at 52°. Samples were measured as prepared, without any pre-treatment.

Transmission electron microscopy (TEM) investigations were performed using a Cs-corrected (S)TEM Themis microscope operating at 200 keV. Samples were drop-casted from ethanol dispersions onto ultrathin carbon films (TED PELLA) onto meshy carbon films on copper grids (Ultrathin, meshy carbon support film, 400 mesh).

Surface microtopography and roughness were further studied by an optical microscope (Keyence VHX-6000, KEYENCE Corporation, Osaka, Japan).

### 2.4. Structural analyses

X-ray diffractometry (XRD) was employed to analyze calcium phosphate phases, using a Bruker AXS D8 Discover instrument. This device included a Cu Kα radiation source ($\lambda = 0.154$ nm), a Göbel mirror, and a Bruker AXS scintillation detector (Karlsruhe, Germany). The instrument's operational settings were 40 kV and 40 mA. Diffraction patterns were acquired within a 2Θ range of 10°–65°, with a scan rate of 0.3°/min and a step size of 0.02°. For the evaluation of patterns and the identification of crystallite phases, Diffrac.Eva software was utilized. For infrared spectroscopic (FT-IR) analyses, the attenuated total reflection (ATR) technique was conducted with a Varian Scimitar 2000 FT-IR spectrometer (Varian Inc., USA). This spectrometer came equipped with an MCT (mercury–cadmium–telluride) detector and a "Golden Gate" single-reflection diamond ATR unit (Specac Ltd., UK). To prepare solid samples, they were pressed firmly onto the diamond crystal by a sapphire anvil exerting a constant force of 70 cNm. Spectra were captured with a nominal resolution of 4 $cm^{-1}$ and involved 128 co-added scans. ATR correction steps were completed before any data evaluation.

### 2.5. Inductively coupled plasma–optical emission spectroscopy (ICP-OES) study

An ICP-OES spectrometer (PerkinElmer Avio 200) was utilized to assess the elemental composition of cAp and fcAp powders and the dissolution behavior of Ca, Mg, Sr, and Zn elements. The measurements were performed in a cyclone spray chamber, with 1 ppm Y serving as the internal standard. Calibration involved a four-point approach, applying standard solutions at concentrations of 0.01, 0.1, 1, and 10 ppm for each element. To analyze elemental composition, powder samples underwent dissolution in 5 mL of 1 N HCl. For determining the dissolution properties of the two composite coating types, samples, each possessing an effective surface area of 100 $cm^2$, were immersed in 50 mL of a sterile, filtered phosphate-buffered saline (PBS) solution (137 mM NaCl, 2.7 mM KCl, 10 mM Na2HPO4, and 1.8 mM KH2PO4, pH 7.2, sourced from Merck, Rahway, New Jersey, USA). Solution samples were then drawn from the supernatant at regular time points of 1, 5, 10, 15, 20, and 30 days.

### 2.6. Corrosion test by electrochemical potentiodynamic measurements

A conventional three-electrode cell setup, controlled by a Gamry 600+ potentiostat (Gamry Instruments, Warminster, PA, USA), was employed for electrochemical assessments. The working electrode consisted of either uncoated or coated metallic implant samples; a platinum wire acted as the counter electrode, and an SCE/KClsat electrode served as the reference. PBS served as the electrolyte solution. Potentiodynamic polarization curves were captured using a 1 mV $s^{-1}$ scan rate. The open-circuit potential (OCP) was monitored for half an hour to ensure stabilization prior to measurement. Anodic curves were obtained by scanning from +50 mV above the OCP up to 2 V. In the electrochemical measurements, a specially designed electrochemical cell setup was used, with the working electrode positioned so that only 1 $cm^2$ of its surface area could come into contact with the electrolyte.

### 2.7. Immersion test for coating degradation

To assess the bioresorbability of PCL-fcAp and CA-fcAp composite non-continuous coatings, an immersion test was conducted. All samples, prepared as 30 mm × 3 mm discs, were submerged in PBS, ensuring a consistent exposed surface area of 10 $cm^2$. Each sample was placed in a separate container with 10 mL of PBS and kept at room temperature for two weeks. Three identical samples of each coating type were utilized at every measurement interval. Weight change was determined using the formula: W% = (Ws – Wd)/Ws × 100%, where Ws represents the initial weight and Wd is the dry weight after 0, 1, 10, 15, 20, and 30 days of immersion. At each designated time, samples were taken out, washed with distilled water, and dried at 50 °C until a constant mass was achieved.

### 2.8. Adhesion test

The adhesion of the coatings to the titanium substrate was assessed using the tape test method, in accordance with European standard EN ISO 2409. The testing procedure involved making incisions in the surface of the samples with an edge knife (Elcometer crosshatch cutter, Elcometer Instruments Ltd., Manchester, UK), creating a grid of cuts in two perpendicular directions. Once the cuts were completed, adhesive tape was hand-pressed onto the sample surface. The tape was then stripped away at roughly a 60-degree angle after a 5-min interval. The samples were categorized according to an adhesion class model by observing the extent of coating loss within the grid of notches. Moreover, the exterior of every sample was examined using a Keyence optical microscope.

### 2.9. Statistical analysis

Differences between experimental groups were analyzed using one-way analysis of variance (ANOVA, Origin 2024, OriginLab Corporation, USA). Tukey's post-hoc test was applied for comparisons of mean values. Statistical significance was defined at $P = 0.05$. Values of $P < 0.05$ were considered statistically significant ($P < 0.05$), and values below 0.01 were considered highly significant ($P < 0.01$). The number of samples per group was N = 3.

## 3. Results and discussion

### 3.1. Morphological characterization of different samples

Extensive morphological evaluations were performed by SEM observations on cellulose acetate polymer layer, PCL polymer layer, pure carbonated apatite powder (cAP), therapeutic component-added apatite powder (fcAP) particles, as well as the fcAp-CA and fcAp-PCL composite layers, and presented in Fig. 1.

As can be observed, the pure cellulose acetate particles show a

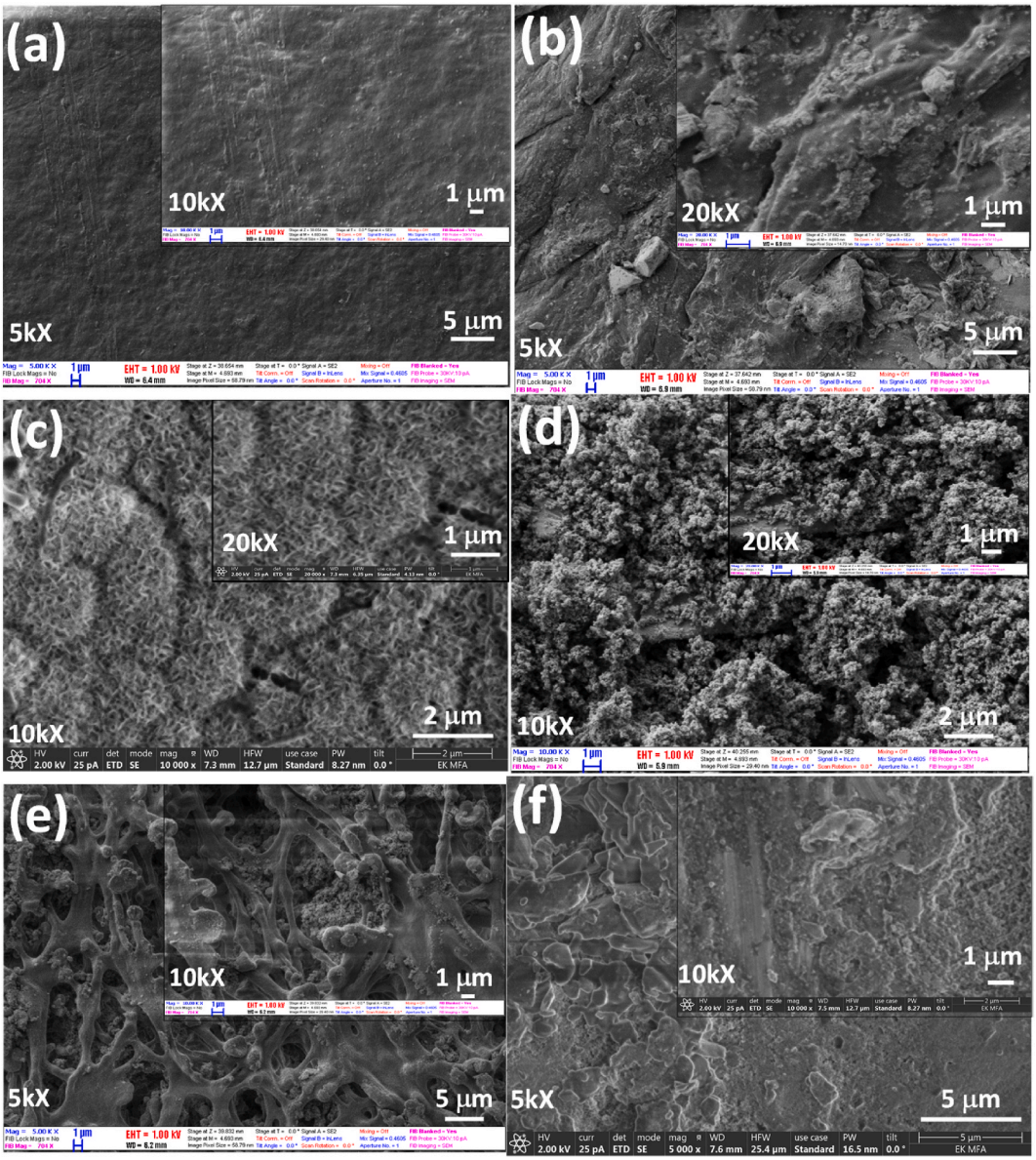


**Fig. 1.** SEM images of cellulose acetate (a), PCL (b), cAp powder (c), fcAp powder (d), fcAp-CA composite (e), and fcAp-PCL composite (f).

uniform morphology, characterized by a smooth surface and the absence of clearly distinguishable particle interfaces (Fig. 1 a). In contrast, the PCL sample displays a heterogeneous surface morphology, consisting of irregularly shaped agglomerates (in the size of 100 nm to 1500 nm) embedded within an amorphous polymeric matrix (Fig. 1 b).

The carbonated apatite powder is composed of elongated nanocrystals that assemble into approximately spherical aggregates with diameters of about 2 µm. The length of the individual cAp particles varies between 100 and 150 nm (Fig. 1 c). This type of nanocrystalline apatite morphology has been widely documented in previous reports [32–34]. The therapeutic compounds visibly altered the morphology of cAP particles (Fig. 1 d). Following functionalization, the powder is dominated by nearly spherical nanoparticles with diameters of approximately 50–100 nm, which tend to aggregate into larger clusters. Fig. 1 (e) and (f) demonstrate the morphology of the fcAP containing biopolymer composites. The fcAP-CA composite (Fig. 1 e) has a unique microstructure, in which the polymer and the fcAP particles can be easily distinguished. The small, rounded fcAP particles are incorporated into the biopolymer, and the particles are surrounded by amorphous CA particles that have an elongated filamentous shape, forming a very porous structure with interconnected pores. In the case of the fcAP-PCL composite, a denser structure is visible, with fewer and smaller pores, compared to the fcAP-CA composite. The larger PCL particles and the smaller fcAP particles are unevenly mixed and can be easily discerned.

Both the elemental mapping and the EDS spectrum have proven the presence of the therapeutic elements within the apatite powder (Fig. 2). The EDS layered image, as well as the elemental mapping, reveal that the magnesium and zinc are homogeneously distributed, while the strontium component is detected in isolated spots in the investigated area.

The cAp and fcAp powder samples were further analyzed by TEM measurements to get a deeper insight into the nanostructure of the particles (Fig. 3).

TEM analysis verified that the cAp powder is composed of crystalline 2D flakes and needle-like structures, measuring 100 nm long and about 10 nm thick. Similarly, the fcAp sample features crystalline needle-shaped particles of equivalent size, alongside detected particles containing Mg, Zn, and Sr. The elemental distribution maps align with the SEM results, showing that Mg and Zn are fairly uniform while Sr is less abundant. Doped particles containing these elements range from 200 to

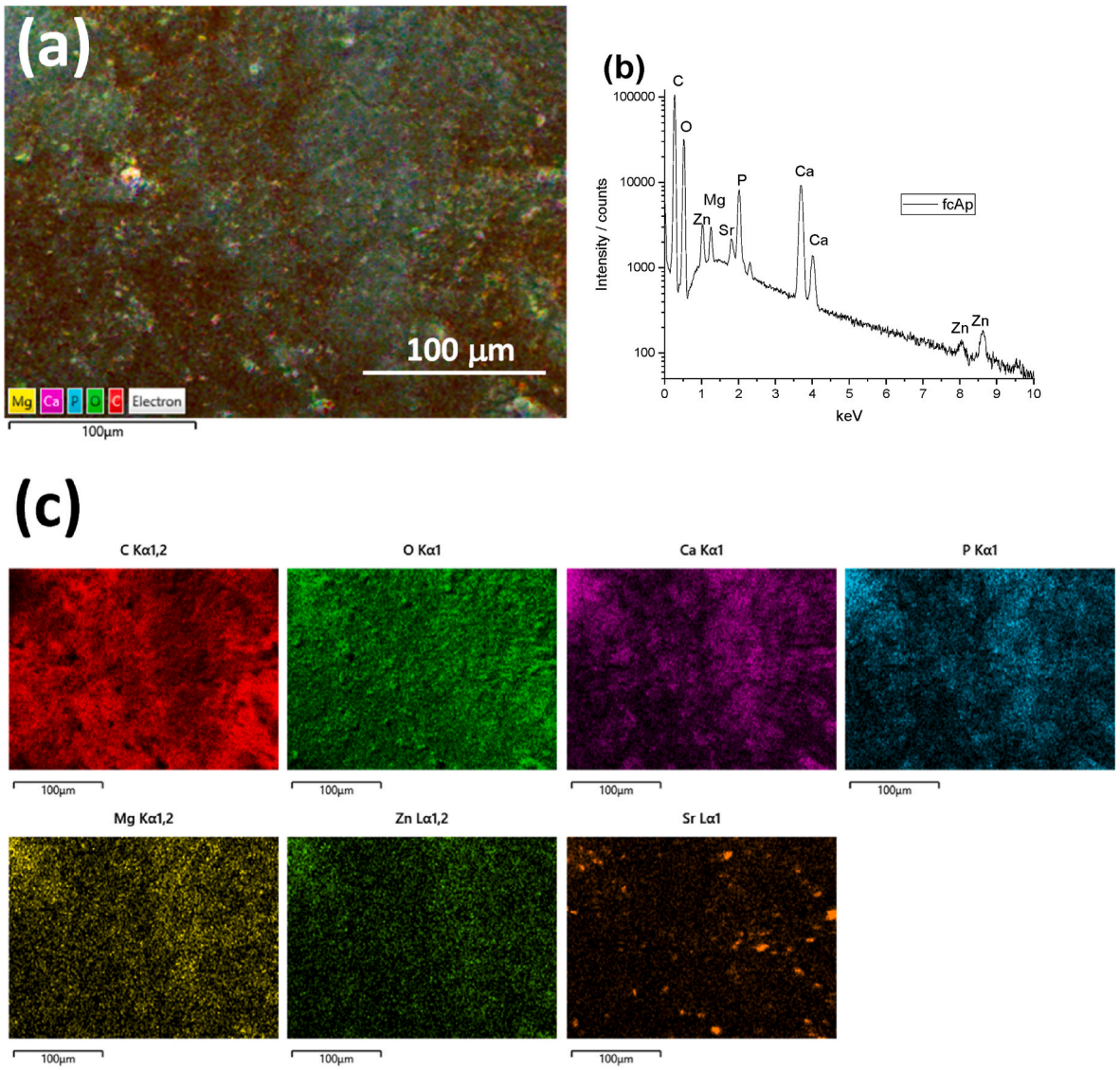


**Fig. 2.** SEM-EDS layered image (a), EDS spectra (b), and elemental mapping of fcAP powder sample (c).

1000 nm in size, though Fig. 3 (d) illustrates that Sr-containing particles sometimes cluster into larger blocks. These specific agglomerates reach sizes between 1 and 5 µm, as seen in Fig. 2 (c) and 3 (d).

The exact elemental compositions of cAp and fcAp were evaluated by ICP-OES technique and are presented in Table 1.

The calculated Ca/P mass ratio was around 2.15 for cAp and 2.07 for fcAp. These ratios are close to the reported elemental ratios in human bones [35,36]. The Ca:Mg:Zn:Sr element ratio was around 65:5:9:21, calculated from the ICP-OES measurements. On the other hand, the nominal elemental ratio calculated from the synthesis feed was 67.5:13.5:8.6:10.4, whereas the mass ratio of the cAp, Mg pidolate, Zn gluconate, and Sr ranelate powders was 3:1:1:1. The differences in values are primarily due to differential recovery of organic metal complexes during acid digestion. While Ca and Zn show excellent agreement (±5%), Mg exhibits significant under-recovery likely due to incomplete dissolution of the organic pidolate ligand. In contrast, Sr-ranelate shows enhanced recovery consistent with its higher acid solubility. These observations confirm successful incorporation of all therapeutic elements, with the observed deviations reflecting standard analytical behavior of organic-inorganic composite materials rather than formulation inconsistencies. However, these differences are moderate and do not undermine the overall statement that the therapeutic elements were successfully incorporated into the fcAp powder at concentrations close to the intended nominal levels.

### 3.2. Structural assessments of cAp and fcAp powders and their composites with PCL and CA polymers

#### 3.2.1. Structural characterization by XRD measurements

The phase compositions of apatite powders and their composites with a synthetic biopolymer, such as PCL, and a naturally derived polymer, such as CA, are presented in Fig. 4.

The XRD pattern of the cAp powder, precipitated from organic Ca gluconate salt, shows a weak and broadened peak between the 2Θ areas of 30 and 33°, which is a merged triple characteristic peaks of hydroxyapatite crystals at 2Θ = 31.7°, 32.2°, and 32.9°. This can indicate that the powder consists of randomly oriented nanocrystals or has a semi-amorphous structure (JCPDS 01-086-1199). A similar structure of nanocrystalline carbonated apatite was described in other papers [37, 38]. Fig. 4 (a) also contains the XRD pattern of the added therapeutic components, such as the Mg pidolate, Sr ranelate, and Zn gluconate. These spectra cannot be found in any available scientific databases; however, it is visible that the Sr and Zn salts are highly crystalline, with sharp and high-intensity peaks. On the other hand, the Mg pidolate has

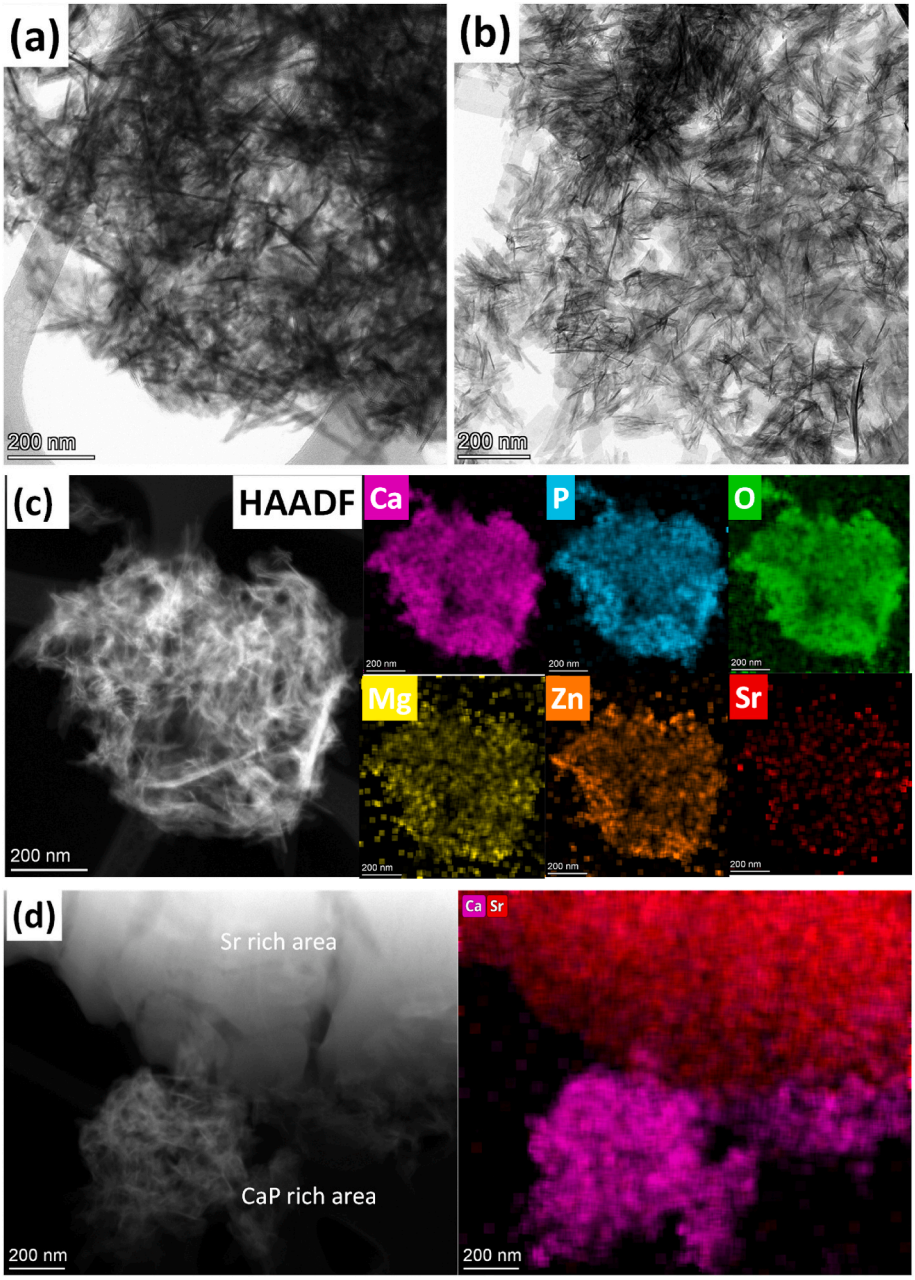


**Fig. 3.** TEM image of cAp powder (a), fcAp powder (b), HAADF (High-Angle Annular Dark-Field) STEM (Scanning Transmission Electron Microscopy) image, and the corresponding elemental mapping on fcAp powder (c) as well as on a specific Sr-rich area of sample (d).

**Table 1**
Concentrations of elements in the cAp and fcAp powders. Mean values (±SD) (N = 3).

| C/mg/L | cAp | fcAP |
|---|---|---|
| Ca | 1103.14 ± 5.4 | 511.38 ± 3.2 |
| P | 515.01 ± 3.5 | 247.02 ± 2.4 |
| Mg | - | 43.32 ± 1.9 |
| Zn | - | 71.75 ± 2.1 |
| Sr | - | 166.15 ± 6.4 |
| Ca/P (Wt%) | 2.14 | 2.07 |
| Ca/P (At%) | 1.65 | 1.60 |

amorphous structure, presenting in two large, broad peaks at around 2Θ = 10°, and 20° As for the mixed fcAp powder, the characteristic broadened peak of nanocrystalline carbonated apatite and the characteristic peaks of the added organic Mg, Zn and Sr salts can also be observed, albeit, in much less intensity. These additional peaks in fcAp cannot be differentiated clearly because they overlap. The XRD pattern of PCL shows sharp diffraction peaks at around 2Θ = 21.4° and 23.7°, which correspond to the (110) and (200) crystal planes, respectively (JCPDS file no. 96-720-5590) [39], indicating its semi-crystalline nature, which means it contains both crystalline and amorphous regions.

In the case of the PCL-fcAp sample, extra peaks appear; a merged broad peak between 2Θ of 31° and 33° region, and a single peak at around 2Θ = 25.7, which can be linked to the amorphous apatite. The characteristic peaks of PCL polymer also remained in the spectrum without significant change. Similar results were obtained in the work of Bauer et al. [40]. They have prepared biomimetic ion-substituted calcium phosphate scaffolds, where the CaP was derived from cuttlefish bone. The CaP powder was doped with $Mn^{2+}$, $Mg^{2+}$, and $Sr^{2+}$ ions in 1, 2.5, and 5 mol%. In their case, there is no significant difference between

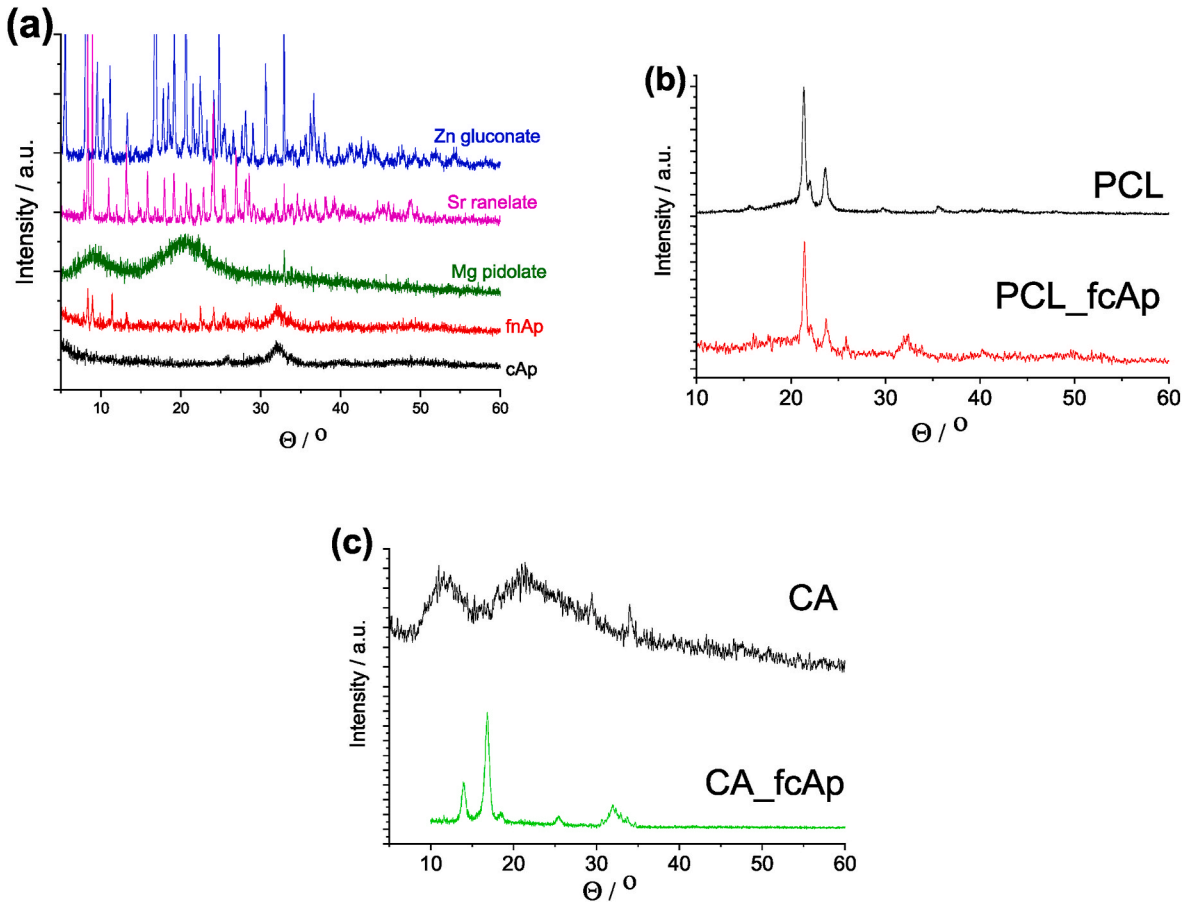


**Fig. 4.** XRD patterns of cAp, fcAp powders along with the therapeutic components (a) and the PCL-fcAp (b), CA-fcAp composites (c).

the XRD patterns of the substituted and non-substituted scaffolds, suggesting that the lattice structure of HAp is not markedly affected by ion substitutions. The same research group, in their earlier work [41], investigated Mg- and Sr-co-substituted calcium phosphate (CaP) scaffolds, with various levels of strontium and magnesium substitution. The CaP powder was impregnated with PCL solution in chloroform. This particular XRD pattern was consistent with crystalline HAp, further revealing the presence of whitlockite in samples that had been substituted with Sr and Mg.

Noticeable XRD variations are present in the CA-based samples, encompassing both the pure polymer and composite forms. Cellulose acetate, a compound derived from cellulose, has specific X-ray diffraction patterns that can elucidate its molecular arrangement and how crystalline it is. These patterns typically display wide peaks, pointing to an amorphous or partially crystalline state. The broadness of these peaks implies a lack of extended structural order, in contrast to the narrow peaks found in highly crystalline materials. The most frequently observed peaks appear at 2Θθ angles of about 12° and 18°, commonly associated with the amorphous areas of cellulose acetate. Furthermore, certain research has reported peaks around 15.70° and 22.44°, providing additional evidence for the presence of amorphous domains within material [42]. These peaks can vary slightly depending on experimental conditions and the specific sample being analyzed. Moreover, the degree of acetylation can also significantly influence the XRD pattern of cellulose acetate. Higher acetylation can lead to a more amorphous structure [43], resulting in broader and less defined peaks in the XRD pattern. This is because increased acetylation disrupts the regular packing of cellulose chains, reducing crystallinity and promoting a more amorphous structure. Besides, the broadened peaks in the XRD pattern can also indicate smaller crystal sizes or the presence of defects in the crystalline structure [44]. In our case, the CA-fcAp composite sample presents a higher degree of crystallinity than the pure CA sample with sharper peaks and higher intensity, in contrast to the PCL-fcAp composite. The extra peaks related to the apatite are also visible in the 31° - 33° 2 theta region (also in Fig. 4 b). In the cases of composite samples (using either CA or PCL matrices), it was observed that the addition of fcAp powder altered the original XRD pattern, affecting the peak positions and intensities.

### 3.2.2. FT-IR measurements on powders and composites

All samples were analyzed by FT-IR measurements to reveal the characteristic groups of the powder and composite materials.

The IR measurement of the cAp sample reflects the spectrum of carbonated apatite (Fig. 5 a).

The apatite $\nu_3PO_4^{3-}$ (1012 $cm^{-1}$) and $\nu_4PO_4$ (doublet at 600 and 560 cm-1) vibrations dominate in the spectrum. The carbonate peaks in carbonate apatite (cAp) appear as stretching vibrations ($\nu$3 and $\nu$4 modes) and bending vibrations ($\nu$2 and $\nu$4 modes). The $\nu$3 mode, related to the carbonate group's CO bond, typically shows strong absorption bands in the 1400-1600 $cm^{-1}$ range, while the $\nu$2 mode (out-of-plane bending) is visible in the 850-900 $cm^{-1}$ range. These bands are specific to cAp and differ from those of non-carbonated hydroxyapatite (HAp), allowing for the detection and quantification of carbonate within the apatite structure [45,46]. The vibrations of the water bands (-OH stretching vibration) appear as a broad peak in the 3500-3300 cm-1 region and can be associated with moisture trapped in the powder samples. In the case of the fcAp sample, the spectrum is slightly different, since the characteristic peaks originating from the organic additives also appeared. For instance, for the magnesium pidolate, which is the magnesium salt of pyroglutamic acid (a

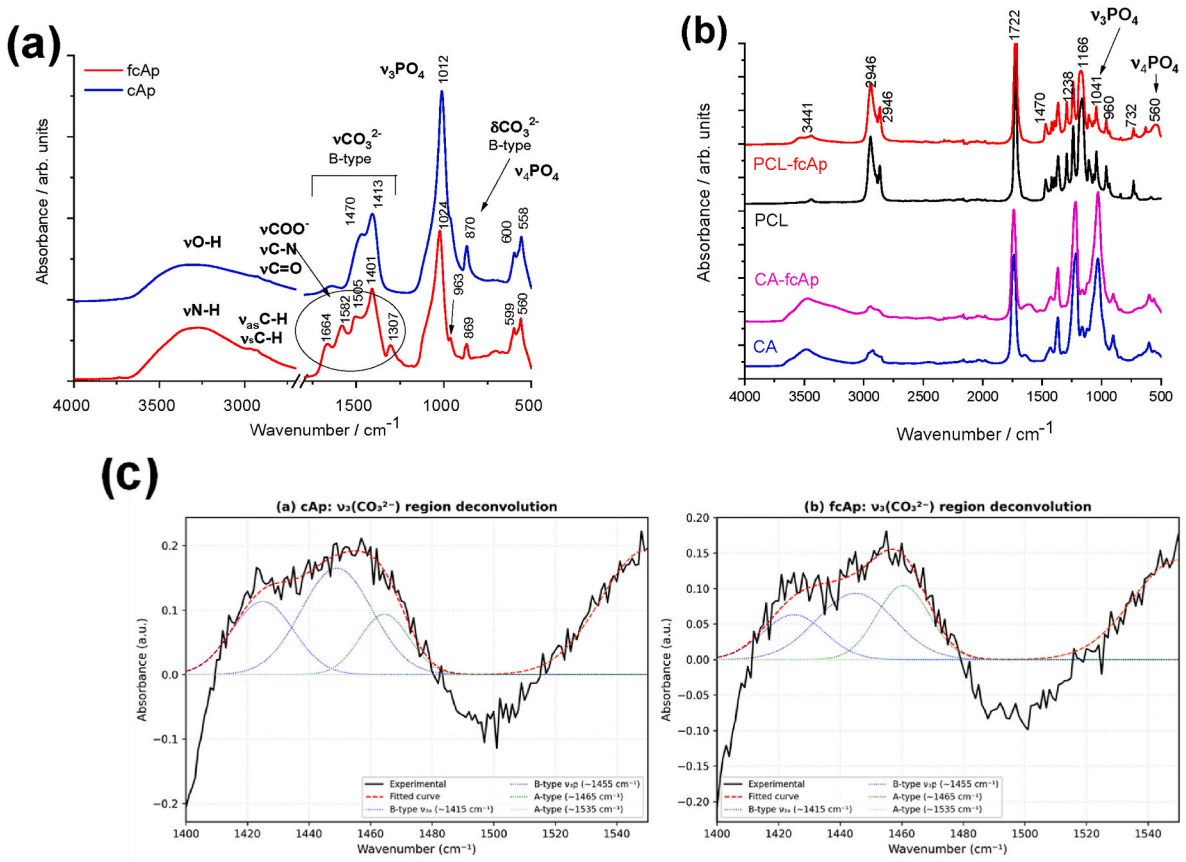


**Fig. 5.** FT-IR spectra of cAp, fcAp powders along with the organic therapeutic components (a) as well as the PCL-fcAp and CA-fcAp composites (b) and FT-IR carbonate deconvolution analysis for your cAp and fcAp samples (c).

pyrrolidone-2-carboxylate), the key infrared-active functional groups are present as a sharp to moderately broad absorption between 3300 and 3500 $cm^{-1}$ (characteristic N–H stretching) [47]. This is visualized in a larger and broader peak compared to the cAp sample. The lactam features a C═O stretch that usually shows up at around 1650–1700 $cm^{-1}$. Carboxylate vibrations, such as asymmetric $COO^-$ stretch at around 1550–1610 $cm^{-1}$, symmetric $COO^-$ stretch at around 1400–1450 $cm^{-1}$, as well as a C–O stretch typically appear between 1300 and 1000 $cm^{-1}$. Additionally, vibrations from the lactam ring, such as C–N stretches around 1250–1000 $cm^{-1}$, C–C ring deformations, and C–O–H vibrations between 1000 and 600 $cm^{-1}$. The general FT-IR features of Zn gluconate are the carboxylate group ($COO^-$) vibrations, asymmetric stretching $\nu(COO^-)$, typically strong at around 1630–1650 $cm^{-1}$, symmetric stretching $\nu(COO^-)$, at around 1400–1420 $cm^{-1}$. Hydroxyl (O–H) stretching at around 3400 $cm^{-1}$, and C–O stretching in alcohol groups appear in the 1000–1100 $cm^{-1}$ region. Additionally, the in-plane O–H bending appears in the 1400–1470 $cm^{-1}$ range, while out-of-plane O–H bending appears near 600–650 $cm^{-1}$ [47]. The Sr ranelate content appears in relevant peaks of its specific functional groups. These peaks originate from carboxylate groups ($COO^-$), such as asymmetric stretch $\nu(COO^-)$ at around 1600–1650 $cm^{-1}$ and symmetric stretch $\nu(COO^-)$ at 1380–1420 $cm^{-1}$ region. The sulfonyl groups (–$SO_2$–), S═O stretching vibrations appears as asymmetric stretch at 1150–1250 $cm^{-1}$ and symmetric stretch at ~1030–1080 $cm^{-1}$, while the aromatic ring vibrations, C═C stretching at ~1500–1600 $cm^{-1}$, C–H in-plane bending at ~1000–1200 $cm^{-1}$ and C–H out-of-plane bending at ~700–900 $cm^{-1}$. Ranelic acid also contains nitrogen in a heteroaromatic form, which appears in C═N stretching at ~1550–1650 $cm^{-1}$; however, this band may overlap with $COO^-$ and aromatic stretches [48,49].

Regarding the composite materials, in the FT-IR spectra of the CA-fcAp sample, only the characteristic bands of CA are dominant, while in the case of the PCL-fcAp sample, the vibrational bands characteristics of apatite are visible along with the characteristic peaks of PCL. For both types of polymers, the fcAp addition did not cause a significant change in the spectrum; they remained identical (Fig. 5 b).

FT-IR deconvolution analysis of the $\nu_2(CO_3^{2-})$ region (850-900 $cm^{-1}$) following the methodology of Madupalli et al. [50] confirms that B-type carbonate substitution ($CO_3^{2-}$ for $PO_4^{3-}$, peak at ~872 $cm^{-1}$) is dominant in both cAp (57.5%) and fcAp (77.0%) samples. Minor A-type contributions (~879 $cm^{-1}$) were also resolved. Using the validated area ratio method described in paper [51], estimated carbonate contents were 3.2-4.8 wt% for cAp and 2.1-3.9 wt% for fcAp, values consistent with synthetic bone-mimetic apatites. The predominance of B-type substitution aligns with the calcium-deficient Ca/P ratios observed and the low-temperature aqueous synthesis conditions, supporting the biomimetic character of these materials for implant coating applications.

### 3.2.3. *Morphological assessment of thin composite coatings on titanium substrates*

The thin layers were deposited onto the surface of titanium via spin coating. The micro and nanostructures of these coatings are presented in Fig. 6.

The SEM image of a commercial titanium implant reveals a very rough microtopography with large, unevenly oriented, sharp metallic particles (Fig. 6 a). It also has deep holes in the investigated area. The CA-coated sample has a completely different morphology (Fig. 6 b). The SEM micrograph reveals a smoother surface with a heterogeneous topography characterized by numerous hemispherical protrusions and crater-like depressions, with diameters ranging from the submicron scale to several micrometers. The overall surface architecture indicates a high degree of porosity and microstructural irregularity, which may arise from gas evolution during the preparation process. The CA-fcAp

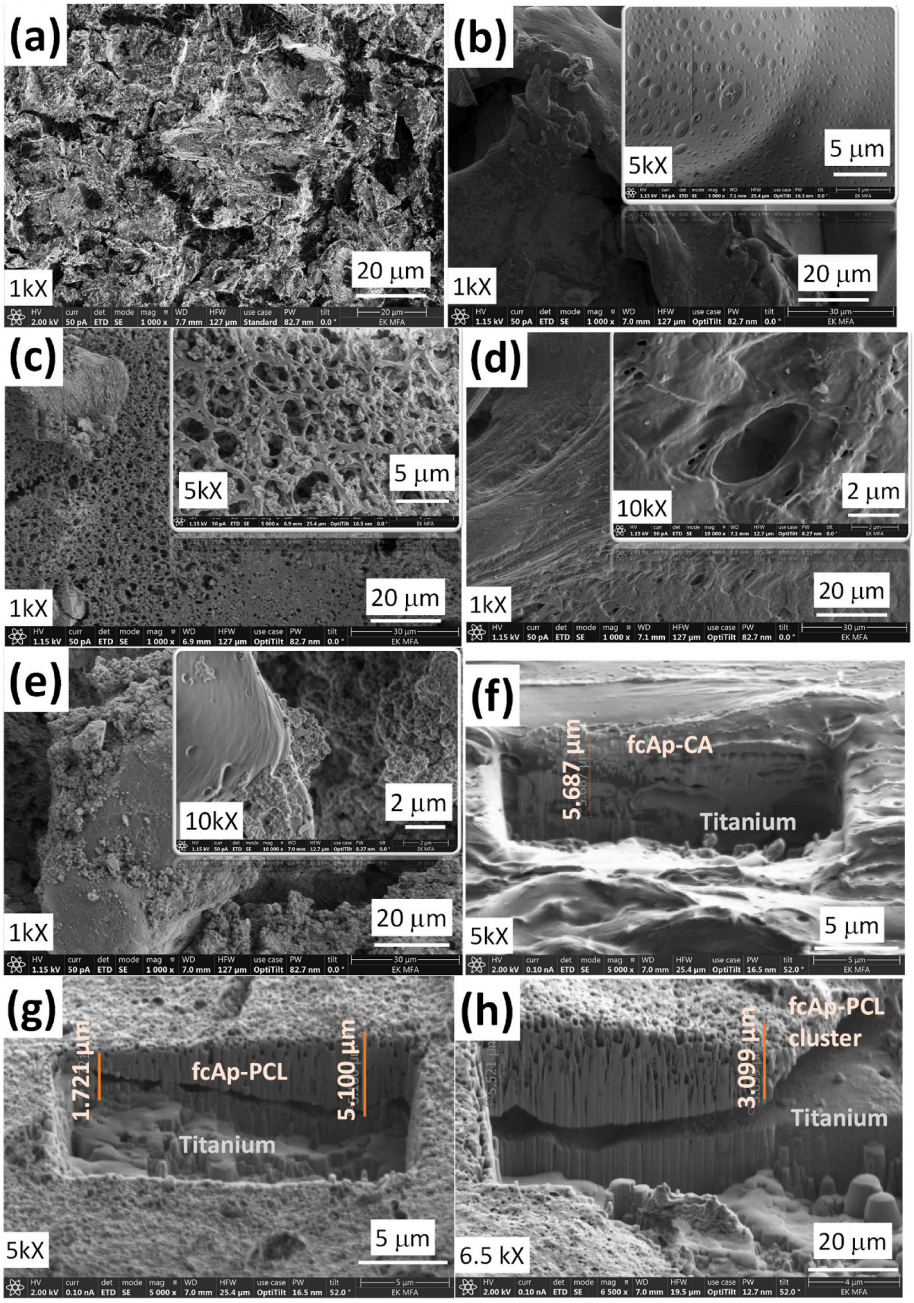


**Fig. 6.** SEM images of uncoated titanium substrate (a), cellulose acetate layer (b), PCL layer (c), fcAp-CA composite layer (d), and fcAp-PCL composite layer (e), SEM-FIB cross-sectional analysis on fcAp-CA composite layer (f) SEM-FIB cross-sectional analysis on fcAp-PCL composite layer (g) and SEM cross-sectional image of the interface fcAp-PCL composite cluster.

composite (Fig. 6 c) has a highly porous structure with interconnected pores. The small fcAp particles are attached to the polymer particles that have mainly fibrous, elongated morphology. This architecture resembles the hierarchical porosity of cancellous bone, producing a highly open and interconnected structure. The pure PCL layer also presents a smooth, amorphous, rippled structure that contains many holes, ranging from nanometers to micrometers in size (Fig. 6 d).

PCL-fcAp composite layer, prepared with the same method, has also heterogeneous micro- and nanostructures. The SEM image (Fig. 6 e) reveals that the smaller fcAp particles are incorporated into the larger, plate-like polymer particles. It is visible in higher magnifications that the small, needle-like fcAp particles are either between the PCL plates or are deposited onto the surface of the PCL plates in discrete areas. The layer also contains several holes and larger cracks.

It is also visible that the microstructures of both composite coatings are highly porous with numerous holes inside. Such porous architecture is expected to promote cellular attachment and proliferation by providing a large accessible surface area [52]. The presence of an interconnected pore system supports mass transport, allowing efficient diffusion of nutrients and oxygen while enabling metabolic waste removal [53–55]. The thickness of the individual composite clusters was studied by FIB cut and SEM measurements. It was proven that the layers in both composites are ultra-thin, varying between 2 and 8 µm. It is also visible that the inner structure of the composites is highly porous with interconnected pores.

The topography and distribution characteristics of the different layers were examined by optical microscope as well (Fig. 7).

Optical microscope images provide an alternative perspective on the

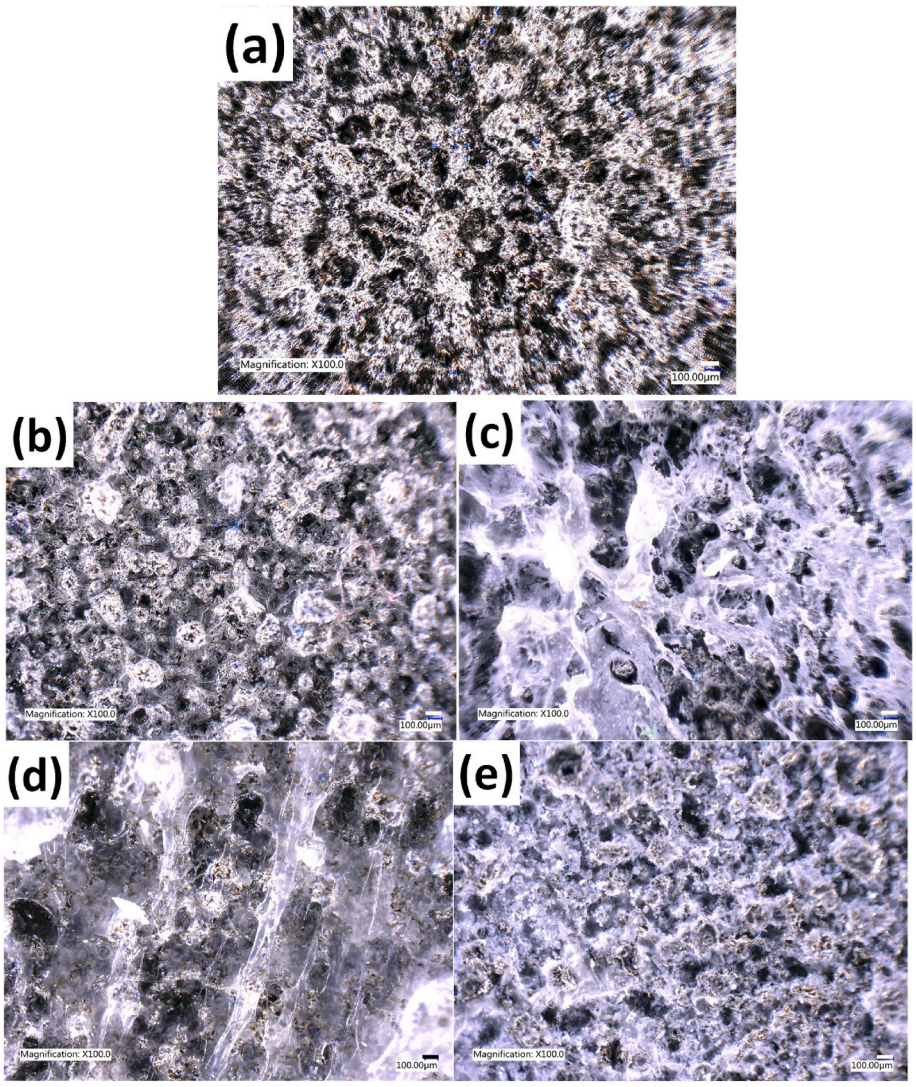


**Fig. 7.** Optical microscope images of uncoated titanium substrate (a), cellulose acetate layer (b), PCL layer (c), fcAp-CA composite layer (d), and fcAp-PCL composite layer (e).

substrate and its various layers. It is visible that all the layers are unevenly distributed across the implant material's rough surface. The layers only partially cover the substrate and appear to be discontinuous. This feature of the structure is beneficial for the biodegradability of layers. As the primary goal of the coating is to accelerate bone growth, it is more advantageous for these coatings to dissolve in the human body concurrently with bone regeneration, facilitating complete recovery [56,57].

The SEM and optical microscopy images (Figs. 6 and 7) confirmed the successful deposition of a non-continuous coating, where composite clusters are distributed across the rough titanium substrate. The observed discontinuity of the coating is an intentional structural characteristic rather than a result of imperfect processing. As hypothesized, this structure is highly beneficial for biodegradability and bone ingrowth. The voids between clusters provide immediate pathways for cell migration and fluid transport, enhancing initial biological integration [54]. Furthermore, this design prevents the formation of a large, continuous polymer-ceramic interface that is prone to cohesive failure under mechanical load [56]. Instead, degradation can be initiated at multiple discrete sites, allowing for a more gradual and harmonious transfer of mechanical support from the resorbing coating to the newly formed bone infiltrating the spaces. This approach aligns with the findings of Ballo et al. [57], who demonstrated that coatings allowing direct bone-implant contact resulted in superior mechanical fixation compared to continuous barrier coatings.

### 3.3. Surface roughness measurements

The roughness of the surface is also a crucial factor for the integration of implants by the human body. It is extensively reported that rougher surfaces are beneficial for the attachment of bone cells [58].

Fig. 8 illustrates the surface macrotopography and roughness measurements on the substrate as well as on different discontinuous coatings.

The roughness profiles confirm the high roughness of the surfaces. It also reveals that the titanium has the roughest surface, while applying thin, non-continuous layers slightly decreased the roughness. This can be attributed to the fact that the coatings, in all cases, tend to accumulate in the deepest parts of the surface.

The parameters of the surface roughness of different samples are shown in Table 2.

According to the RzJIS values, which give the average of the five highest peaks and five deepest valleys within a specified sampling length on a roughness profile, the largest peak-to-valley distance, 138 µm, was observed for titanium, contrasting with the lowest values found in polymer-coated samples (both CA and PCL). Composite coatings

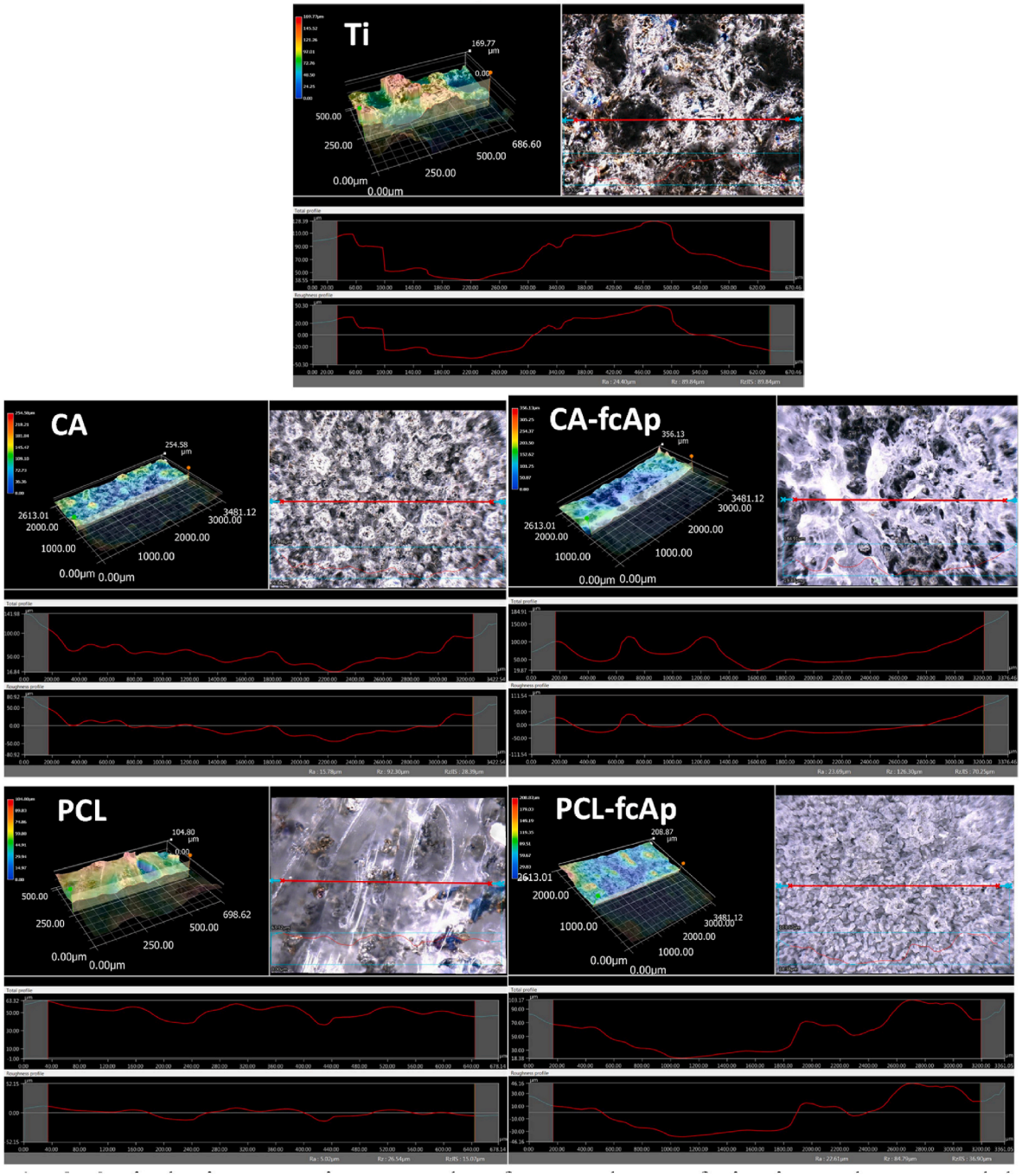


**Fig. 8.** Optical microscope images and surface roughness of Titanium substrate, and the non-continuous coatings of CA polymer, CA-fcAp composite, PCL polymer, as well as PCL-fcAp composite.

**Table 2**
Surface roughness parameters from the line profile of the investigated samples. Parameters are presented as arithmetic average roughness (Ra), the largest difference from peak-to-valley (Rz), RzJIS (surface roughness parameter), maximum profile peak height (Rp), and the maximum profile valley depth (Rv). The surface roughness was scanned at six different line profiles, and the mean values ± SD are presented (N = 6).

| Samples | Ra/µm | Rz/µm | RzJIS/µm | Rp/µm | Rv/µm |
|---|---|---|---|---|---|
| Titanium | 30.29 ± 4.22 | 156.14 ± 11.98 | 138.80 ± 13.61 | 105.65 ± 9.96 | 70.49 ± 8.32 |
| CA layer | 18.69 ± 2.19 | 126.31 ± 15.01 | 70.25 ± 7.44 | 72.80 ± 5.26 | 53.52 ± 7.41 |
| CA-fcAp | 26.24 ± 5.25 | 132.38 ± 12.17 | 121.44 ± 11.73 | 114.71 ± 15.39 | 77.67 ± 9.26 |
| PCL layer | 20.02 ± 3.41 | 96.85 ± 7.64 | 66.03 ± 8.77 | 50.90 ± 6.74 | 45.95 ± 4.68 |
| PCL-fcAp | 25.94 ± 4.39 | 99.82 ± 8.98 | 112.87 ± 12.84 | 99.35 ± 11.65 | 68.88 ± 9.55 |

exhibited increased roughness, but their values were not higher than those of the bare substrate. It is noted that surface roughness and

hydrophilicity are directly related, which promotes better osteoblast spreading and differentiation [58,59].

The roughness measurements can also determine the specific surface volume of different samples. The surface area investigated was 10 $mm^2$ for all samples, and the values are demonstrated in Table 3.

It has been shown by roughness measurements that the uncoated titanium surface exhibits the highest volume, whereas the non-continuous coatings consistently caused a small decrease in the available surface area. This outcome can be attributed to the accumulation of both polymer and composite coatings within the deeper valleys of the surface.

### 3.4. Corrosion and degradability tests

#### 3.4.1. Tafel evaluation

Electrochemical measurements can determine the corrosion rate of implant materials. The curves were recorded at a 1 mV/s scanning rate, spanning ±150 mV from the open circuit potential (OCP). To achieve an equilibrium state, the OCP was monitored for 30 min. From the intersection points of the cathodic and anodic Tafel curve slopes, the current densities ($j_{corr}$) and corrosion potentials ($E_{corr}$) for each material were ascertained.

As Fig. 9 and Table 4 illustrate, the uncoated substrate displayed the most negative corrosion potential, indicating heightened electrochemical activity. In this case, elevated corrosion currents were also recorded, a consequence of the larger electrochemically active surface area interacting with the electrolyte. Conversely, the polymer-based discontinuous composite layers exhibited slightly reduced corrosion currents, suggesting fewer charge-transfer processes. This is attributable to the partial coverage of the samples' surface by a non-conductive composite layer. The electrochemical corrosion assessments confirmed that the coating hindered the release of Ti4+ from the implant material, a finding consistent with reported corrosion measurements for both hydroxyapatite and polymer composite coatings [60,61].

The corrosion rate generally correlates linearly with the corrosion current density, as determined from the polarization curves. The potentiodynamic variables and the linear polarization resistance (Rp) were computed within the ±50 mV potential window around the corrosion potential (Ecorr) using the simplified Stern–Geary equation (1). The Rp for titanium was minimal, whereas the maximum value was observed for the CA-fcAp partially coated titanium. Fundamentally, Rp is inversely proportional to the uniform corrosion rate.

$$R_p = \frac{B}{j_{corr.}}, \quad (1)$$

where $B = 0.026V$ constant, $j_{corr}$ is corrosion current density (in A/$cm^2$)

The corrosion rate can also be calculated with equation (2), which gives the mass of corrosion product in g/($cm^2$·s).

$$CR = \frac{j_{corr.}\ x\ EW}{nxF} \quad (2)$$

and CR × 3.1536 × $10^{10}$, in mg/year dimension.

where CR is the corrosion rate (in g/$cm^2$·s), $j_{corr}$ is corrosion current density (in A/$cm^2$), EW is the equivalent weight (in g/mol), for titanium,

**Table 3**
3D roughness parameters of different samples. Sa is the arithmetical mean height, Sz is the maximum height, Sq is the root mean square height within the evaluation area of 10 $mm^2$.

| Samples | Sa/μm | Sz/μm | Surface volume/$mm^3$ |
|---|---|---|---|
| Titanium | 36.94 | 148.95 | 1.09 |
| CA layer | 17.04 | 118.63 | 0.77 |
| CA-fcAp | 36.07 | 126.15 | 0.89 |
| PCL layer | 17.23 | 104.82 | 0.68 |
| PCL-fcAp | 30.08 | 112.60 | 0.91 |

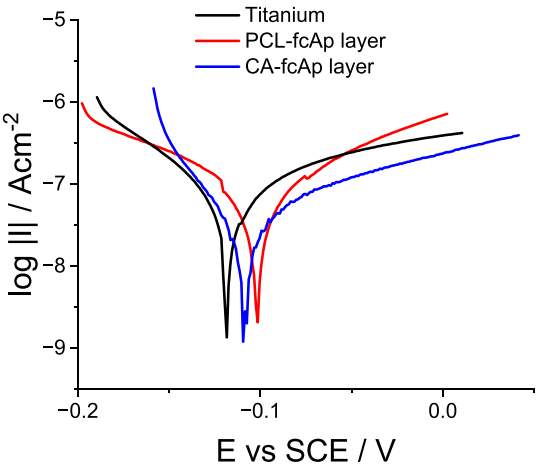


**Fig. 9.** Tafel curves of uncoated titanium, PCL-fcAp composite layer and CA-fcAp composite layer recorded after 30 min of electrolyte stabilization in PBS. The scanning rate was 1 mV/s ± 150 mV from the open circuit potential (OCP).

**Table 4**
Corrosion parameters of different samples by evaluation of Tafel curve.

| Sample | $E_{corr}$/mV | $j_{corr}$/nAcm$^{-2}$ | Rp/kΩcm$^2$ | CR/mgcm$^{-2}$yr$^{-1}$ |
|---|---|---|---|---|
| Titanium | −116 | 39.46 | 658.89 | 0.154 |
| PCL-fcAp | −102 | 33.11 | 785.26 | 0.123 |
| CA-fcAp | −108 | 21.37 | 1216.65 | 0.083 |

it is 11.9675 g/mol n is the number of electrons transferred, and F is Faraday's constant (96,485 C/mol)

It's important to note that fcAp, being a ceramic material, undergoes degradation primarily through solution equilibria, involving dissolution/precipitation in PBS, rather than electron transfer; therefore, in this case, Faradaic charge transfer is inapplicable.

#### 3.4.2. Electrochemical potentiodynamic measurements

The potentiodynamic curves were recorded over a large potential range in the anodic region to observe the possible surface passivation processes. Three replicate samples were measured after 1 day, 10 days, 20 days, and 30 days of immersion in PBS solutions.

Potentiodynamic curves were acquired over a wide potential range, extending to anodic potentials of +2 V. As illustrated in Fig. 10, the anodic branch of the titanium sample exhibits a wide and well-defined passive region, with passivation initiating at approximately +200 mV. The reproducibility of the curve profiles over time confirms the electrochemical stability of the surface. A slight decrease in passive current density during the anodic sweep indicates progressive stabilization of the passive film. Passive layer breakdown occurs at approximately +1.5 V, marked by a sharp increase in current density.

In contrast, partially coated titanium samples display distinctly different polarization behavior, attributable to their heterogeneous surface composition and structural complexity. These samples exhibit an extended passive region commencing at approximately +50 mV; however, passive film breakdown occurs at lower potentials, around +1.2 V, for both composite coatings.

For coated systems, the passive region becomes increasingly unstable with rising overpotential. Repeated breakdown and re-passivation events are observed between +300 and + 600 mV for the PCL-fcAp–titanium sample and between +100 and + 300 mV for the CA-fcAp–titanium sample, indicating localized disruption of the passive layer during anodic polarization. Furthermore, the pronounced slopes of the anodic branches across all samples suggest that the electrode processes are governed by a combination of charge-transfer kinetics and

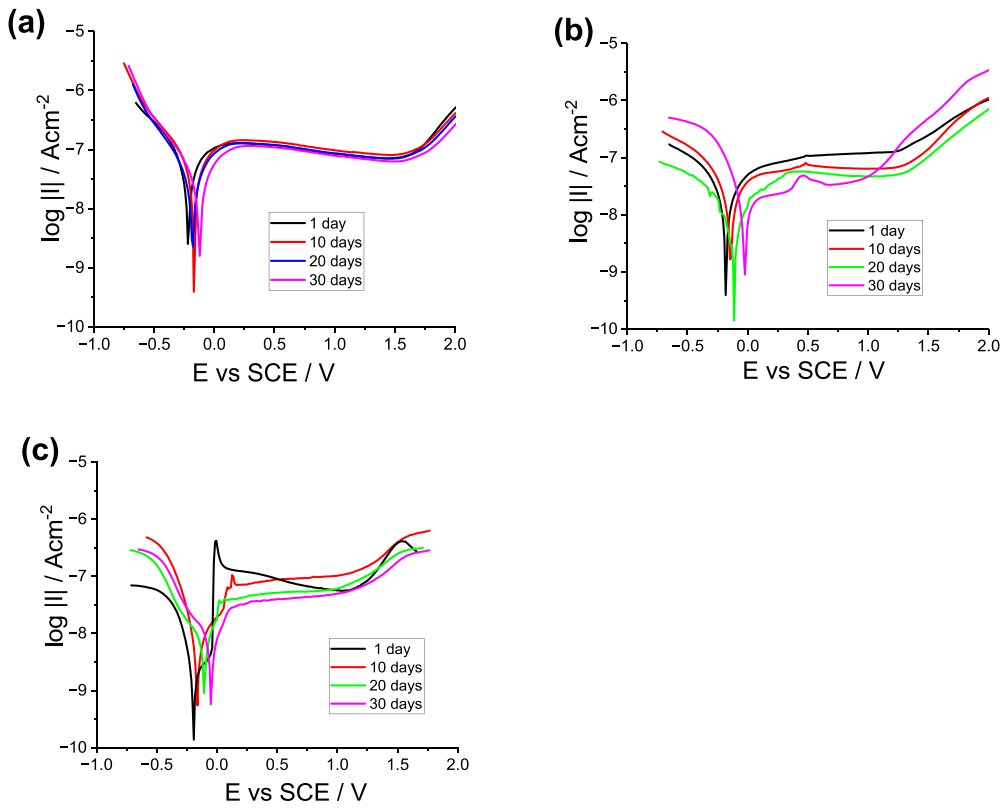


**Fig. 10.** Potentiodynamic polarization curves of uncoated Titanium (a), PCL-fcAp-coated titanium (b), and CA-fcAp-coated titanium (c) recorded several times over a month in PBS. The potential scanning rate was 1 mV $s^{-1}$ in each case.

mass transport limitations.

The time dependence of corrosion potentials, corrosion current

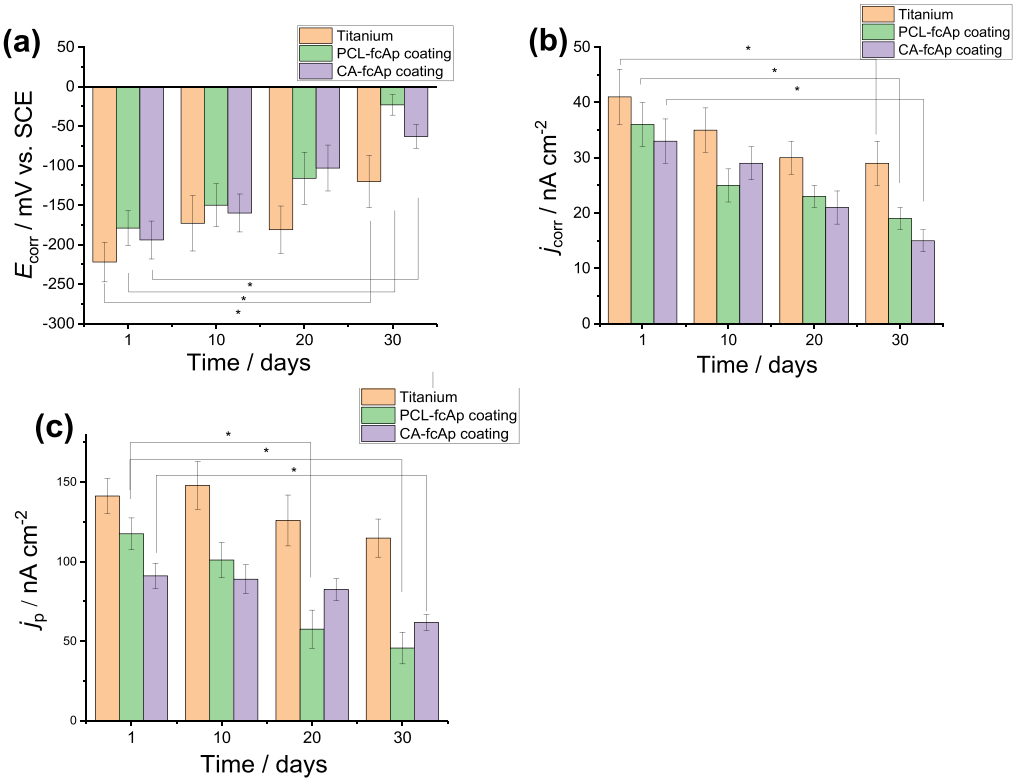


**Fig. 11.** Electrochemical parameters: $E_{corr}$ (a), $j_{corr}$ (b) and $j_p$ (c) derived from the potentiodynamic curves in Fig. 10. Values are graphed as the mean ± standard deviation ($N = 3$). * Indicates $P < 0.05$ (statistically different).

densities ($j_{corr}$), passive current densities ($j_p$) at 0.5 V overpotential are presented in Fig. 11.

As illustrated in Fig. 11 (a), the corrosion potential ($E_{corr.}$) values for each material type progressively shifted towards more positive potentials over time. The uncoated implant consistently showed more negative corrosion potentials, signifying a more electrochemically active surface.

As depicted in Fig. 11 (b), the corrosion current density (jcorr.) values were derived from the intersection of lines extrapolated from the cathodic and anodic branches of the potentiodynamic curves found in the Tafel region, a method analogous to that in Fig. 9. The corrosion current densities of the uncoated implant were observed to decrease gradually over time; however, both composite coatings exhibited a marginally faster reduction in their measured jcorr values. The PCL-based composite's jcorr values diminished steadily but slowly during the immersion period, while the CA-based composite coated sample initially showed a swift decline in its corrosion current, followed by a deceleration that led to a semi-saturated curve. Additionally, the titanium uncoated substrate registered the lowest passive current densities, which barely fluctuated over the immersion time (Fig. 11 c).

The $j_p$ values for both ceramic coating types were lower than those of the substrate. Over time, particularly during the initial immersion period, the passive currents of the PCL-based composite coating diminished more considerably, indicating superior surface passivation compared to the CA-based composite coating. This passivation could stem from corrosion products that form while immersed in PBS solution, potentially sealing the coating's pores and thereby hindering dissolution. A statistical analysis of the $E_{corr}$, $j_{corr}$, and $j_p$ values demonstrated that only those measured after a month of immersion showed a statistically significant difference. These corrosion figures are consistent with other studies on the corrosion rates of titanium [62], hydroxyapatite-based coatings [61], and certain composite coatings [63].

Vranceanu et al. [61], for instance, utilized an electrochemical method to deposit and assess hydroxyapatite material layers infused with Mg or Zn ions. They discovered that these ceramic applications produced diminished corrosion current readings compared to the nanostructured titanium substrate, thus demonstrating their protective nature, independent of the electrolyte type. Importantly, all HAp-based coatings presented an increased level of the polarization resistance (Rp) parameter (changing from 160 $k\Omega cm^{-1}$ to 691 $k\Omega cm^{-1}$, depending on the coating composition). In other research [63], multiwalled carbon nanotubes containing HAp-chitosan composite coating were electrophoretically deposited onto a titanium surface. The composite coating displayed significant corrosion resistance, characterized by a corrosion current of about 9 nA/cm2.

### 3.5. Immersion tests

Given that electrochemical methods are unsuitable for measuring the degradation mechanism of polymers and composites (there are no electron/charge transfer reactions), we quantified the alterations in composite weight after a month of submersion in PBS to monitor the biodegradability features of composite coatings.

Fig. 12 (a) illustrates a modest time-dependent increase in weight loss for both composite coatings. Specifically, the PCL-fcAp composite coating experienced an initial phase of negligible deterioration, followed by a slightly accelerated rate of degradation after two weeks of immersion, yet its weight loss barely reached 0.5%. Conversely, the CA-based composite exhibited robust stability in inert physiological media, with a mere 0.15% weight loss recorded during the experimental duration. These experiments collectively demonstrate that PCL- and CA-based composites undergo moderate degradation in neutral environments. Numerous sources in the literature indicate that PCL degradation occurs slowly through ester bond hydrolysis in physiological (in vitro) settings [7], though its biodegradation rate is reportedly boosted by enzymatic catalysis in vivo, facilitating its absorption [7].

For instance, Dias et al. [64] studied the degradation characteristics of electrospun PCL both in vitro and in vivo. They concluded that PCL had minimal mass loss over weeks to months in buffered physiological media. For example, one study observed only about 1.4% weight loss after 90 days in phosphate-buffered saline at 37 °C.

Under physiological conditions, the full resorption of PCL is a process that extends over several years. Literature suggests that the complete in vivo degradation of bulk PCL or its breakdown in buffered media typically takes around 2 to 4 years [65]. An in vitro study also estimated that a PCL multifilament yarn would fully decompose in approximately 14 months in PBS at 37 °C [66]. Conversely, the degradation process for CA polymer and CA-based composites is more involved, requiring deacetylation and specific enzymatic reactions. In purely abiotic PBS conditions, the primary degradation pathway for CA is the hydrolysis of its acetate ester side groups [67]. However, without particular enzymes, its degradation is not substantial. As a result, in vitro and in enzyme-free PBS, the polymer backbone of CA remains largely unaltered over time [67]. Numerous studies affirm CA's high resistance to hydrolytic breakdown at 37 °C in neutral pH, and its degradation characteristics are also influenced by its macro- and microstructure, its crystallinity, molecular mass, and the degree of substitution [68]. In a 16-week test in near-neutral water, a cellulose acetate film lost only around 2.5% of its weight, while a fibrous CA lost around 2.3% [69]. Cellulose acetate largely retains its mass under rigorous in vitro conditions (sterile PBS without enzymes); typically, no detectable weight loss is observed over periods of several weeks or even months. Researchers have reported that cellulose acetate's stability is so high that it persisted with essentially its original mass and shape for months in soil-burial tests, which also include natural microbes [70]. Conversely, the fcAp ceramic component of composites undergoes ionic dissolution and precipitation, governed by its extremely low solubility product constants for calcium phosphate phases in neutral environments; therefore, its degradation rate is determined by the surrounding polymer matrix.

As illustrated in Fig. 12b and c, the ion-release profiles show the liberation of ions over a one-month period in PBS at a pH of 7.4 and room temperature. Both composite materials exhibit an initial rapid release of ions during the first five days, followed by a more gradual, continuous release for up to 30 days. Specifically, the PCL-fcAp composite demonstrated a significant rise in Ca concentration, reaching approximately 50 μg/L after two weeks of immersion, subsequently stabilizing. In contrast, the CA-fcAp composite exhibited lower Ca ion levels, around 40 μg/L after a month, which can be attributed to CA's enhanced stability under the neutral conditions studied (as depicted in Fig. 12 a). The Ca ion release pattern for both composite types resembles a saturation curve, likely due to potential precipitation/dissolution processes involving the formation of insoluble calcium phosphate precipitates (with phosphate ions derived from the PBS solution).

The patterns we observed, showing an initial quick release followed by a leveling off, are characteristic of CaP bioceramics; for example, one PCL/Mg-phosphate scaffold released most of its Ca and $PO_4^{3-}$ in the first week, then continued at a reduced pace until 21 days [71]. While our findings generally match established data on cumulative release curves [72,73], the release behaviors for $Mg^{2+}$, $Zn^{2+}$, and $Sr^{2+}$ are notably different. All bioactive ion concentrations increased gradually in both composites, with the rapid initial rise of $Mg^{2+}$ and $Zn^{2+}$ attributed to the high solubility of their organic compounds in water during early immersion. These ion concentrations showed no signs of saturation over a month.

The steep increase at the beginning of immersion was caused by the leaching of surface-bonded Mg and Zn ions, followed by a slower increase up to 30 days, consistent with the polymer matrix degradation rate. This steady and continuous increase, without a sharp plateau, indicates ongoing Mg and Zn leaching. Other scientific reports note that $Mg^{2+}$ often displays a strong initial release in buffered solutions due to its good solubility [73]. Literature also indicates that significant $Zn^{2+}$ release usually requires higher Zn content. For instance, one review

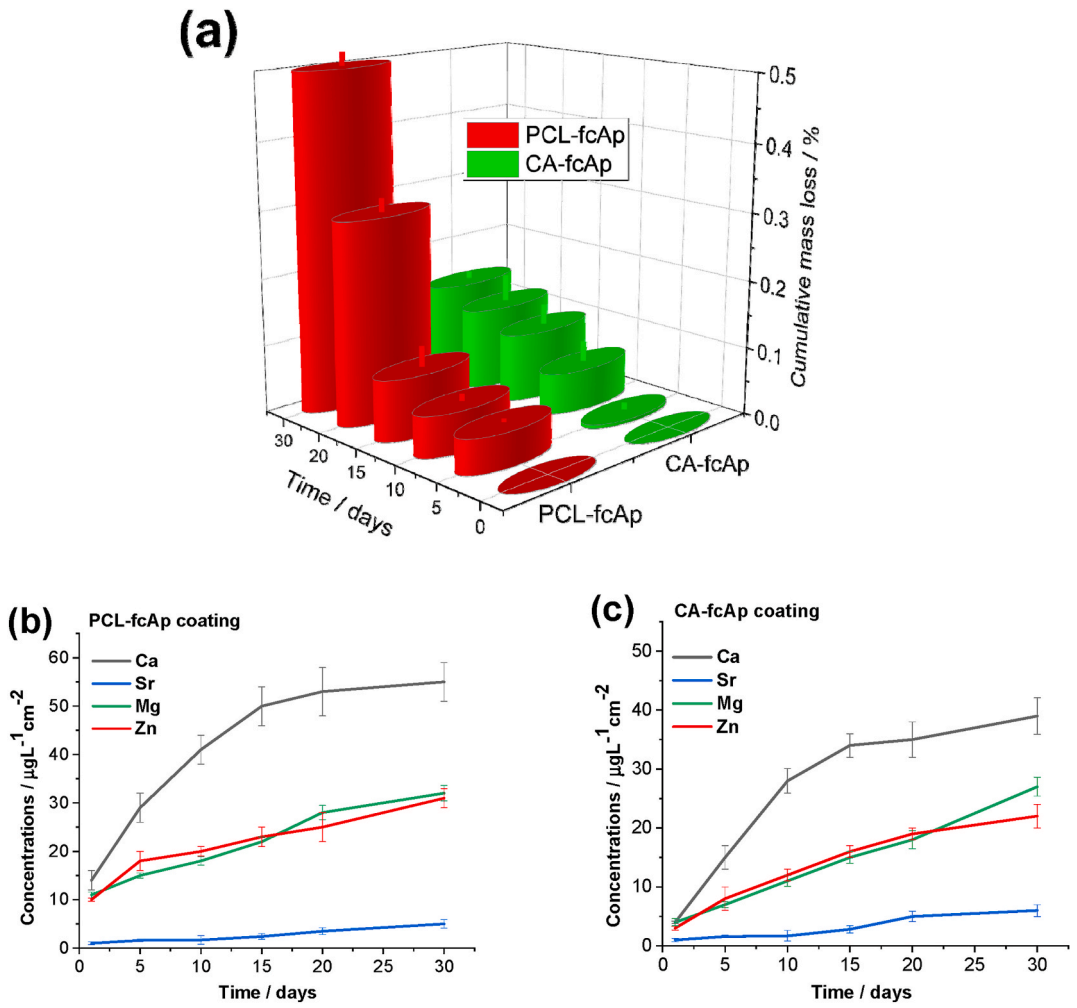


**Fig. 12.** Cumulative normalized sample weight loss in percentage during the one-month immersion period in PBS at room temperature (a), cumulative concentrations of the dissolved Ca, Sr, Mg and Zn from PCL-fcAp coating (b) and CA-fcAp (c) coating immersed in PBS solution at room temperature. The values are normalized to the unit area of the samples. Values are graphed as the mean ± standard deviation (N = 3).

notes $Zn^{2+}$ leaching from Zn-doped HA in PBS was only evident for high Zn substitution, from 5 to 20 wt% [74]. The slow Zn release is typical in substituted calcium phosphate phases in biological environments [75]. Conversely, the strontium concentration released was considerably lower, by a factor of 4-6, in both samples. This limited Sr release can be attributed to the low water solubility of the strontium ranelate component within the composite materials, which only becomes available as the polymer degrades. Literature supports this, indicating that $Sr^{2+}$ release from Sr-containing HAp is generally slow; for instance, one study observed only 14–18% of Sr content leached over 14 days in PBS [76]. Our data, spanning over 30 days, confirm a strong retention of $Sr^{2+}$. Such controlled Sr release is common and delivers a sustained, low-dose $Sr^{2+}$ stimulus, preventing environmental overload [77]. Immersion studies quantitatively demonstrated a greater release of all ions from the PCL-fcAp composite. For example, calcium release was approximately 20% higher in PCL-fcAp, while magnesium and zinc releases were about 15-20% greater. This finding could suggest that a cellulose acetate polymer is capable of forming stronger bonds with ions, thereby inhibiting their diffusion. We also observe that polymer crystallinity, porosity, and water absorption can impact ion leaching: PCL is semi-crystalline and hydrophobic, though its porous microstructure may enable fluid access, whereas cellulose acetate might swell differently. In summary, both composites exhibit similar kinetic patterns, including an initial burst (attributed to the dissolution of loosely bound apatite and therapeutic elements on the polymer's external surfaces) and a subsequent slower release (due to internal diffusion and reprecipitation phenomena). The plateauing of calcium levels indicates local saturation and the reprecipitation of apatite on the implant surface [73].

During immersion tests and ion-release studies, our composite materials demonstrated one month of stability in static, neutral environments. However, a significant limitation is the current absence of exact biological validation, which constitutes the next stage of our investigation. Although Sr, Mg, and Zn were incorporated for their recognized biological roles [21,23], actual cellular responses still await scrutiny. Consequently, our results introduce a materials platform with potential bioactivity, rather than a clinically approved coating. Furthermore, the basic in vitro arrangement for analyzing degradation and corrosion fails to accurately simulate dynamic biological environments. Phosphate-buffered saline lacks enzymes, proteins, or cellular activity that substantially alter the degradation rates of both biopolymer matrices and the ceramic phase in living systems [64,67].

The stability observed for CA or PCL-based coatings in PBS is unlikely to persist under physiological conditions, where esterase activity could hasten their breakdown. Consequently, the measured degradation rates and ion release characteristics should be considered as preliminary data from controlled environments, rather than reliable indicators of in vivo performance. Nevertheless, our positive electrochemical and morphological results are a vital and advantageous prerequisite for clinical application.

In essence, this study provides a foundational protocol for the

synthesis and characterization of novel composite coatings. Although the data regarding their structure, in vitro corrosion resistance, and degradation in a neutral solution are significant, their practical application is limited by the experimental setup. The true biological effectiveness and mechanical strength of these coatings are still unknown, and their clinical viability can only be confirmed once these vital subsequent investigations are successfully completed.

### 3.6. Adhesion evaluation of ultra-thin, non-continuous composite coatings on titanium substrate

Fig. 13 supports a Class 0/no flaking or detachment outcome for both coatings after the tape adhesion test, because the cut pattern remains visible and the coating appears intact without obvious edge lifting, peeling, delamination, or coating loss in the cross-hatched area. The composite coatings remained firmly attached after tape removal, which indicates excellent coating adhesion and strong interfacial cohesion to the substrate, corresponding to a best-performance adhesion class in the cross-cut test. Similar adhesion test methods on ion-doped calcium phosphate-based coatings were reported and summarized in the review work of Fosca et al. [78] in which they compared the factors influencing the adhesion strengths to the substrate.

### 3.7. Architectural advantages of non-continuous coatings

The spin-coated composite layers in this study were intentionally engineered to be non-continuous or discrete (Figs. 6 and 7). This architectural choice offers several functional advantages over conventional continuous coatings, which are widely documented in the literature [27,28,57]. It is reported that continuous thick coatings, such as plasma-sprayed hydroxyapatite (HAp), are prone to delamination, cohesive failure, and particulate debris, especially under cyclic loading. For example, plasma-sprayed HA coatings on titanium alloys are widely used but are prone to delamination [79]. In contrast, our discrete composite clusters are attached to the roughened titanium substrate only at separated sites. This configuration distributes interfacial stresses and reduces the risk of catastrophic coating detachment, as each cluster behaves independently. The continuous coatings inevitably mask or alter the native micro- and nano-topography of the titanium substrate, which is known to profoundly influence osteoblast behavior [80]. By covering only a fraction of the surface, our non-continuous design preserves the original roughness, surface energy, and topographical features of the titanium substrate while adding the bioactivity of the fcAp filler. Besides, the voids between composite clusters provide immediate pathways for host bone cells and fluids to reach the exposed titanium substrate, enabling early contact osteogenesis. In the case of a continuous coating, the entire coating must first be resorbed or infiltrated before direct bone–implant contact can be established, which can significantly delay osseointegration. This discrete architecture enables a graduated and harmonious load transfer from the resorbing coating to the newly forming bone. As the polymer-fcAp clusters degrade, the voids are progressively filled by ingrowing bone. Stress is transferred incrementally from the coating to the bone, avoiding the sudden loss of mechanical support that can occur when a continuous coating delaminates or dissolves unevenly [81]. Collectively, these considerations, supported by the extensive literature on implant surface engineering, validate our intentional design of a non-continuous composite coating. While a direct experimental comparison with a uniform continuous coating is outside the scope of the present work, the clear advantages of the discrete architecture provide a strong rationale for this design.

## 4. Conclusions

Carbonated apatite powder (cAp) was produced using wet chemical precipitation and then blended with therapeutic organic Mg, Zn, and Sr components to create fcAp. This powder mixture was subsequently integrated into two kinds of biopolymers: a synthetic PCL and a natural derivative CA. The composite material was then deposited as non-continuous layers onto a commercially available, roughened titanium substrate through spin coating. Morphological characterization of cAp particles revealed that they were made up of small, thin, needle-shaped particles arranged into large spherical forms, roughly 2 μm in size.

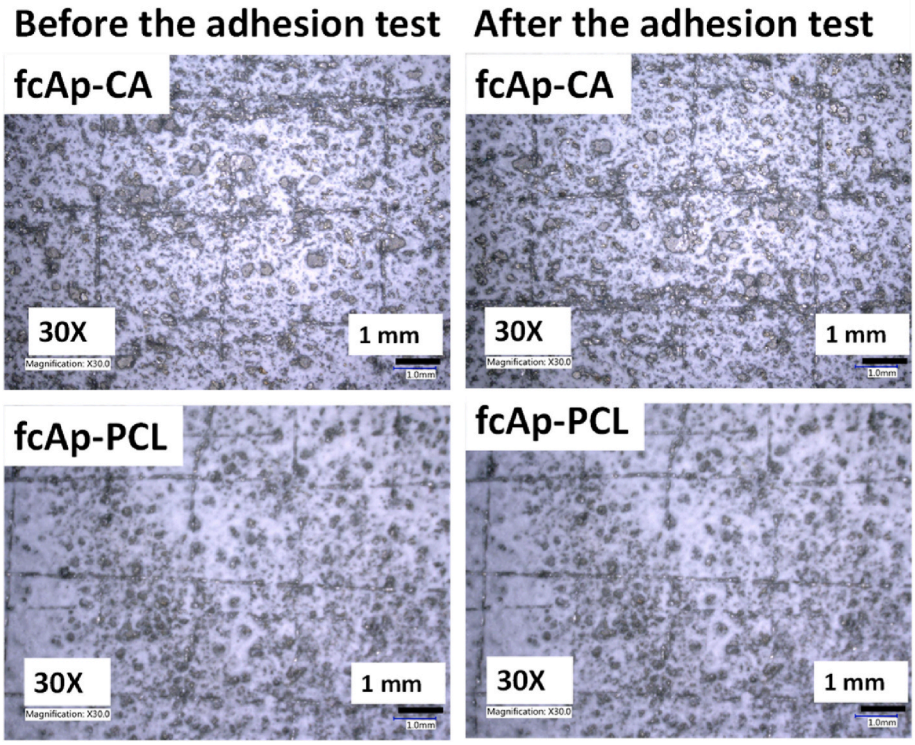


**Fig. 13.** Cross-cut tape adhesion assessment of fcAp-CA and fcAp-PCL coatings on titanium according to EN ISO 2409.

Individual cAp particles were measured between 100 and 150 nm in length. On the other hand, the fcAp powder mainly comprised small, rounded particles, approximately 50 - 100 nm in size, which tended to accumulate into larger blocks of various sizes and shapes. TEM measurements confirmed these morphologies.

The micro-morphology of pure biopolymers was smooth with amorphous particles. For the composites, fcAP particles were embedded into the biopolymer matrices and formed a very porous structure with interconnected pores in each case. The optical microscope evaluations confirmed the layers to be discontinuous.

Structural analyses, including XRD and FT-IR, confirmed the powders to be mainly B-type carbonated apatite, as evidenced by the combination of phosphate and carbonate bands in the FT-IR spectra and the characteristic broadened apatite peaks in the XRD patterns. The retention of the organic therapeutic ingredients within the biopolymer matrices was further confirmed by the appearance of their characteristic FT-IR bands (such as N–H stretching and carboxylate vibrations) in the composite spectra, in good agreement with the spectra of the pure compounds.

Electrochemical potentiodynamic measurements yielded low corrosion current densities ($j_{corr}$ = 21-39 nA/cm$^2$ across all samples), which decreased by 20-46% for the partially coated samples relative to uncoated titanium. These values are consistent with excellent corrosion resistance for titanium-based implant materials in physiological media and demonstrate the protective effect of the non-continuous bioactive coatings. This observation is attributed to the formation of a passive layer on the surface and the reduced electrochemically active area volume in the coated samples. Sustained potentiodynamic measurements indicated that a robust passive layer was maintained for over a month in PBS immersion.

The degradation rate of composite coatings was tested by immersing the samples in PBS solution for one month. The results showed very low degradation for both PCL-based and CA-based coatings; however, with different degradation characteristics. While the PCL had a slight decrease in mass after two weeks of immersion, after that, the mass loss slightly increased linearly. On the other hand, the CA-based coating hardly changed over time; its mass loss did not exceed 0.15% weight loss, which is negligible. This slow degradation rate is explained by the neutral environment without enzymes that could catalyze the decomposition of biopolymers.

Overall, our findings confirmed the successful synthesis of a novel fcAp powder and its integration into PCL and CA matrices, resulting in coatings with a bone-mimetic, porous morphology, improved electrochemical stability, and controlled, slow degradation in a neutral medium.

## Declaration of competing interest

The authors declare that they have no known competing financial interests or personal relationships that could have appeared to influence the work reported in this paper.

## Acknowledgment

The Authors are grateful for the SEM measurements to Z. Kovács and T. Kolonits, for the ICP-OES measurement to I. Tolnai, for the FT-IR measurements to J. Mihály, Zs. Kasztovszky and V. Szilágyi, and for the XRD measurements for Zs. E. Horváth. This work was supported by the National Research, Development and Innovation Office – NKFIH OTKA-FK 146141. The authors also thanks the support of VEKOP-2.3.3-15-2016-00002 of the European Structural and Investment Funds.

## References

[1] Wu H, Chen X, Kong L, Liu P. Mechanical and biological properties of titanium and its alloys for oral implant with preparation techniques: a review. Materials 2023;16(21):6860. https://doi.org/10.3390/ma16216860.
[2] Stich T, Alagboso F, Křenek T, Kovářík T, Alt V, Docheva D. Implant-bone-interface: reviewing the impact of titanium surface modifications on osteogenic processes in vitro and in vivo. Bioeng Transl Med 2021;7(1):e10239. https://doi.org/10.1002/btm2.10239.
[3] Nikolova MP, Apostolova MD. Advances in multifunctional bioactive coatings for metallic bone implants. Materials 2022;16(1):183. https://doi.org/10.3390/ma16010183.
[4] Mostafa AA, Oudadesse H, Mohamed MB, Foad ES, Le Gal Y, Cathelineau G. Convenient approach of nanohydroxyapatite polymeric matrix composites. Chem Eng J 2009;153(1–3):187–92. https://doi.org/10.1016/j.cej.2009.05.039.
[5] Du M, Chen J, Liu K, Xing H, Song C. Recent advances in biomedical engineering of nano-hydroxyapatite including dentistry, cancer treatment and bone repair. Composites, Part B Eng 2021;215:108790. https://doi.org/10.1016/j.compositesb.2021.108790. ISSN 1359 – 8368.
[6] Ganbaatar SE, Kim H-K, Kang N-U, Kim EC, U HJ, Cho Y-S, Park H-H. Calcium phosphate (CaP) composite nanostructures on polycaprolactone (PCL): synergistic effects on antibacterial activity and osteoblast behavior. Polymers 2025;17:200. https://doi.org/10.3390/polym17020200.
[7] Cidade do Carmo C, Brito M, Oliveira JP, Marques A, Ferreira I, Baptista AC. Cellulose acetate and polycaprolactone fibre coatings on medical-grade metal substrates for controlled drug release. Polymers 2024;16(14):2006. https://doi.org/10.3390/polym16142006.
[8] Liu W, Cheong N, He Z, Zhang T. Application of hydroxyapatite composites in bone tissue engineering: a review. J Funct Biomater 2025;16(4):127. https://doi.org/10.3390/jfb16040127.
[9] Furko M. Bioglasses versus bioactive calcium phosphate derivatives as advanced ceramics in tissue engineering: comparative and comprehensive study, current trends, and innovative solutions. J Funct Biomater 2025;16(5):161. https://doi.org/10.3390/jfb16050161.
[10] Habraken WJEM, Wolke JGC, Jansen JA. Ceramic composites as matrices and scaffolds for drug delivery in tissue engineering. Adv Drug Deliv Rev 2007;59(4–5):234–48. https://doi.org/10.1016/j.addr.2007.03.011.
[11] Archer E, Torretti M, Madbouly S. Biodegradable polycaprolactone (PCL) based polymer and composites. Phys Sci Rev 2023;8(11):4391–414. https://doi.org/10.1515/psr-2020-0074.
[12] Romão S, Bettencourt A, Ribeiro IAC. Novel features of cellulose-based films as sustainable alternatives for food packaging. Polymers 2022;14(22):4968. https://doi.org/10.3390/polym14224968.
[13] Benito-Kaesbach A, Beltrán-Sanahuja A, Mathers RT, Sanz-Lázaro C. Understanding the degradation of bio-based polymers across contrasting marine environments using complementary analytical techniques. J Clean Prod 2025;524:146435. https://doi.org/10.1016/j.jclepro.2025.146435.
[14] Visan AI, Popescu-Pelin G, Socol G. Degradation behavior of polymers used as coating materials for drug Delivery-A basic review. Polymers 2021;13(8):1272. https://doi.org/10.3390/polym13081272.
[15] Bangratz M, Guinobert I, Dubourdeaux M, Guilbot A. Higher absorption and lower urinary elimination of a new magnesium rice complex compared to two other organic forms of magnesium: a pilot study in rats. Food Nutr J 2016;1:107. https://doi.org/10.29011/2575-7091.100007.
[16] Bertinato J, Plouffe LJ, Lavergne C, Ly C. Bioavailability of magnesium from inorganic and organic compounds is similar in rats fed a high phytic acid diet. Magnes Res 2014;27(4):175–85. https://doi.org/10.1684/mrh.2014.0374.
[17] Tokarczyk J, Koch W. Dietary Zn—recent advances in studies on its bioaccessibility and bioavailability. Molecules 2025;30(13):2742. https://doi.org/10.3390/molecules30132742.
[18] Tahir M, Khan N, Fatima M, Haque NU, Davies SJ. Bioavailability of zinc from different organic zinc chelates and their effect on the growth, whole body, tissue zinc content, enzymes activity and proximate composition of L. rohita. PLoS One 2025;20(3):e0314146. https://doi.org/10.1371/journal.pone.0314146.
[19] Stefanelli LF, Alessi M, Bertoldi G, Rossato V, Di Vico V, Nalesso F, Calò LA. Calcineurin-inhibitor-induced hypomagnesemia in kidney transplant patients: a monocentric comparative study between sucrosomial magnesium and magnesium pidolate supplementation. J Clin Med 2023;12:752. https://doi.org/10.3390/jcm12030752.
[20] Maier JA, Pickering G, Giacomoni E, Cazzaniga A, Pellegrino P. Headaches and magnesium: mechanisms, bioavailability, therapeutic efficacy and potential advantage of magnesium pidolate. Nutrients 2020;12(9):2660. https://doi.org/10.3390/nu12092660.
[21] Mehta D, Gentleman E. Advances in strontium-releasing biomaterials for bone repair. Biomaterials 2026;326:123718. https://doi.org/10.1016/j.biomaterials.2025.123718. ISSN 0142-9612.
[22] Horák P, Skácelová M, Kazi A. Role of strontium ranelate in the therapy of osteoporosis. J Rheum Dis Treat 2017;3:50. https://doi.org/10.23937/2469-5726/1510050.
[23] Molenda M, Kolmas J. The role of zinc in bone tissue health and Regeneration—A review. Biol Trace Elem Res 2023;201:5640–51. https://doi.org/10.1007/s12011-023-03631-1.
[24] Dehghanpour AA, Rouhi G. A critical review on the effects of dental implants micro-roughness on osseointegration. Biomed Mater Dev 2025. https://doi.org/10.1007/s44174-025-00454-7. n. pag.

[25] Luo J, Walker M, Xiao Y, Donnelly H, Dalby MJ, Salmeron-Sanchez M. The influence of nanotopography on cell behaviour through interactions with the extracellular matrix - a review. Bioact Mater 2021;15:145–59. https://doi.org/10.1016/j.bioactmat.2021.11.024.
[26] Smeets R, Stadlinger B, Schwarz F, Beck-Broichsitter B, Jung O, Precht C, Kloss F, Gröbe A, Heiland M, Ebker T. Impact of dental implant surface modifications on osseointegration. Biomed Res Int 2016;2016:6285620. https://doi.org/10.1155/2016/6285620.
[27] Matteo M, Tommasini V, Rubini K, Boi M, Baldini N, Boanini E. State of art and perspective of calcium phosphate-based coatings coupled with bioactive compounds for orthopedic applications. Nanomaterials 2025;15:1199. https://doi.org/10.3390/nano15151199.
[28] Tang W, Fischer NG, Kong X, Sang T, Ye Z. Hybrid coatings on dental and orthopedic titanium implants: current advances and challenges. BMEMat 2024;2(4):e12105. https://doi.org/10.1002/bmm2.12105.
[29] Xia B, Liu Y, Xing Y, Shi Z, Pan X. Biodegradable medical implants: reshaping future medical practice. Adv Sci 2025;12(35):e08014. https://doi.org/10.1002/advs.202508014.
[30] Zhang Z, Zhong X, Li L, Hu J, Peng Z. Unmasking the delamination mechanisms of a defective coating under the co-existence of alternating stress and corrosion. Prog Org Coating 2023;180:107560. https://doi.org/10.1016/j.porgcoat.2023.107560.
[31] Kubiak-Mihkelsoo Z, Kostrzębska A, Błaszczyszyn A, Pitułaj A, Dominiak M, Gedrange T, Nawrot-Hadzik I, Matys J, Hadzik J. Ionic doping of hydroxyapatite for bone regeneration: advances in structure and properties over two decades—A narrative review. Appl Sci 2025;15:1108. https://doi.org/10.3390/app15031108.
[32] Furko M, Horváth ZE, Mihály J, Balázsi K, Balázsi C. Comparison of the morphological and structural characteristic of bioresorbable and biocompatible hydroxyapatite-loaded biopolymer composites. Nanomaterials 2021;11:3194. https://doi.org/10.3390/nano11123194.
[33] Yotsova R, Peev S. Biological properties and medical applications of carbonate apatite: a systematic review. Pharmaceutics 2024;16(2):291. https://doi.org/10.3390/pharmaceutics16020291.
[34] Szterner P, Antosik A, Pagacz J, Tymowicz-Grzyb P. Morphology control of hydroxyapatite as a potential reinforcement for orthopedic biomaterials: the hydrothermal process. Crystals 2023;13(5):793. https://doi.org/10.3390/cryst13050793.
[35] Sotiropoulou P, Fountos G, Martini N, Koukou V, Michail C, Kandarakis I, Nikiforidis G. Bone calcium/phosphorus ratio determination using dual energy X-ray method. Phys Med 2015;31(3):307–13. https://doi.org/10.1016/j.ejmp.2015.01.019.
[36] Harkness JS, Darrah TH. From the crust to the cortical: the geochemistry of trace elements in human bone. Geochem Cosmochim Acta 2019;249:76–94. https://doi.org/10.1016/j.gca.2019.01.019.
[37] Wang B, Zhang Z, Pan H. Bone apatite nanocrystal: crystalline structure, chemical composition, and architecture. Biomimetics 2023;8(1):90. https://doi.org/10.3390/biomimetics8010090.
[38] Solodyankina A, Nikolaev A, Frank-Kamenetskaya O, Golovanova O. Synthesis and characterization of nanocrystalline apatites from solution modeling human blood. J Mol Struct 2016;1119:484–9. https://doi.org/10.1016/j.molstruc.2016.04.080.
[39] Abdelrazek EM, Hezma AM, El-khodary A, Elzayat AM. Spectroscopic studies and thermal properties of PCL/PMMA biopolymer blend, Egypt. J Basic Appl Sci 2016;3(1):10–5. https://doi.org/10.1016/j.ejbas.2015.06.001.
[40] Bauer L, Antunović M, Ivanković H, Ivanković M. Biomimetic scaffolds based on $Mn^{2+}$-, $Mg^{2+}$-, and $Sr^{2+}$-Substituted calcium phosphates derived from natural sources and polycaprolactone. Biomimetics 2024;9(1):30. https://doi.org/10.3390/biomimetics9010030.
[41] Bauer L, Antunović M, Gallego-Ferrer G, Ivanković M, Ivanković H. PCL-coated multi-substituted calcium phosphate bone scaffolds with enhanced properties. Materials 2021;14(16):4403. https://doi.org/10.3390/ma14164403.
[42] Ezzat D, Youssif M, Elhaes H, El-Nahass M. XRD and UV–Vis studies of cellulose acetate film blended with different concentrations of nano-metal oxide. Opt Quant Electron 2024;56:839. https://doi.org/10.1007/s11082-024-06480-x.
[43] Raza A, Farrukh S, Hussain A, Khan I, Othman MHD, Ahsan M. Performance analysis of blended membranes of cellulose acetate with variable degree of acetylation for CO2/CH4 separation. Membranes 2021;11(4):245. https://doi.org/10.3390/membranes11040245.
[44] Huda E, Rahmi Khairan. Preparation and characterization of cellulose acetate from cotton. IOP Conf Ser Earth Environ Sci 2019;364:012021. https://doi.org/10.1088/1755-1315/364/1/012021.
[45] Hong SI, Lee KH, Outslay ME, Kohn DH. Ultrastructural analyses of nanoscale apatite biomimetically grown on organic template. J Mater Res 2008;23:478–85. https://doi.org/10.1557/JMR.2008.0051.
[46] Ren F, Ding Y, Leng Y. Infrared spectroscopic characterization of carbonated apatite: a combined experimental and computational study. J Biomed Mater Res 2014;102(2):496–505. https://doi.org/10.1002/jbm.a.34720.
[47] Li Y, Yan Z, Liu J, Song C, Zhu F, Wang S. The evaluation of *bacillus*-secreted polyglutamic acid as anti-scaling treatment for circulating cooling water. Environ Sci Pollut Res 2022;29:82762–71. https://doi.org/10.1007/s11356-022-21299-3.
[48] Aparecida da Rosa J, Sakane KK, Panelli Santos KC, Bradaschia Corrêa V, Arana-Chavez VE, Xavier de Oliveira J. Strontium ranelate effect on the repair of bone defects and molecular components of the cortical bone of rats. Braz Dent J 2016;27(5):502–7. https://doi.org/10.1590/0103-6440201600693.
[49] Farlay D, Boivin G, Panczer G, Lalande A, Meunier PJ. Long-term strontium ranelate administration in monkeys preserves characteristics of bone mineral crystals and degree of mineralization of bone. J Bone Miner Res 2005;20:1569–78. https://doi.org/10.1359/JBMR.050405.
[50] Madupalli H, Pavan B, Tecklenburg MMJ. Carbonate substitution in the mineral component of bone: discriminating the structural changes, simultaneously imposed by carbonate in A and B sites of apatite. J Solid State Chem 2017;255:27–35. https://doi.org/10.1016/j.jssc.2017.07.025.
[51] Brangule A, Gross KA. Importance of FTIR spectra deconvolution for the analysis of amorphous calcium phosphates. IOP Conf Ser Mater Sci Eng 2015;77:012027. https://doi.org/10.1088/1757-899X/77/1/012027.
[52] Farjaminejad S, Farjaminejad R, Garcia-Godoy F. Nanoparticles in bone regeneration: a narrative review of current advances and future directions in tissue engineering. J Funct Biomater 2024;15(9):241. https://doi.org/10.3390/jfb15090241.
[53] Coburn B, Salary RR. Mechanical characterization of porous bone-like scaffolds with complex microstructures for bone regeneration. Bioengineering 2025;12(4):416. https://doi.org/10.3390/bioengineering12040416.
[54] Murphy CM, O'Brien FJ. Understanding the effect of mean pore size on cell activity in collagen-glycosaminoglycan scaffolds. Cell Adhes Migrat 2010;4(3):377–81. https://doi.org/10.4161/cam.4.3.11747.
[55] Mukasheva F, Adilova L, Dyussenbinov A, Yernaimanova B, Abilev M, Akilbekova D. Optimizing scaffold pore size for tissue engineering: insights across various tissue types. Front Bioeng Biotechnol 2024;12:1444986. https://doi.org/10.3389/fbioe.2024.1444986.
[56] Mehdikhani-Nahrkhalaji M, Fathi MH, Mortazavi V, Mousavi SB, Akhavan A, Haghighat A, Hashemi-Beni B, Razavi SM, Mashhadiabbas F. Biodegradable nanocomposite coatings accelerate bone healing: in vivo evaluation. Dent Res J 2015;12(1):89–99. https://doi.org/10.4103/1735-3327.150342.
[57] Ballo AM, Ågren EK, Bjursten LM, Thomsen P. *In vivo* response to a novel nanostructured titanium coating. Acta Biomater 2012;8(2):889–96. https://doi.org/10.1016/j.actbio.2011.10.023. 2012.
[58] Zhang Y, Fan Z, Xing Y, Jia S, Mo Z, Gong H. Effect of microtopography on osseointegration of implantable biomaterials and its modification strategies. Front Bioeng Biotechnol 2022;10:981062. https://doi.org/10.3389/fbioe.2022.981062.
[59] Zhao G, Raines AL, Wieland M, Schwartz Z, Boyan BD. Requirement for both micron- and submicron scale structure for synergistic responses of osteoblasts to substrate surface energy and topography. Biomater 2007;28(18):2821–9. https://doi.org/10.1016/j.biomaterials.2007.02.024.
[60] Amirnejad M, Rajabi M, Jamaati R. Electrodeposition of hydroxyapatite coating on Ti6Al4V alloy: mechanistic investigation of the substrate crystallographic texture effect. J Electrochem Soc 2022;169(7):072508. https://doi.org/10.1149/1945-7111/ac82c8.
[61] Vranceanu DM, Ungureanu E, Ionescu IC, Parau AC, Pruna V, Titorencu I, Badea M, Gălbău C-Ş, Idomir M, Dinu M, et al. In vitro characterization of hydroxyapatite-based coatings doped with Mg or Zn electrochemically deposited on nanostructured titanium. Biomimetics 2024;9:244. https://doi.org/10.3390/biomimetics9040244.
[62] Hrir H, Layachi OA, Boudouma A, El Bouari A, Sidimou AA, El Marrakchi M, Khoumri E. Electrochemical corrosion behavior of α-titanium alloys in simulated biological environments (comparative study). RCS Adv 2024;14:38110–9. https://doi.org/10.1039/D4RA05869K.
[63] Chandra Rath P, Singh BP, Besra L, Bhattacharjee S. Multiwalled carbon nanotubes reinforced hydroxyapatite-chitosan composite coating on Ti metal: corrosion and mechanical properties. J Am Ceram Soc 2012;95(9):2725–31. https://doi.org/10.1111/j.1551-2916.2012.05195.x.
[64] Dias JR, Sousa A, Augusto A, Bártolo PJ, Granja PL. Electrospun polycaprolactone (PCL) degradation: an in vitro and in vivo study. Polymers 2022;14:3397. https://doi.org/10.3390/polym14163397.
[65] Barnthip N, Teeka J, Kantha P, Teepoo S, Damjuti W. Fabrication and characterization of polycaprolactone/cellulose acetate blended nanofiber mats containing sericin and fibroin for biomedical application. Sci Rep 2022;12:22370. https://doi.org/10.1038/s41598-022-26908-2.
[66] Deshpande MV, Girase A, King MW. Degradation of Poly(ε-caprolactone) resorbable multifilament yarn under physiological conditions. Polymers 2023;15(18):3819. https://doi.org/10.3390/polym15183819.
[67] Tan J, Liang Y, Sun L, Yang Z, Xu J, Dong D, Liu H. Degradation characteristics of cellulose acetate in different aqueous conditions. Polymers 2023;15(23):4505. https://doi.org/10.3390/polym15234505.
[68] Abrusci C, Marquina D, Santos A, Del Amo A, Corrales T, Catalina F. Biodeterioration of cinematographic cellulose triacetate by Sphingomonas paucimobilis using indirect impedance and chemiluminescence techniques. Int Biodeterior Biodegrad 2009;63:759–64. https://doi.org/10.1016/j.ibiod.2009.02.012.
[69] Cragg SM, Beckham GT, Bruce NC, Bugg TD, Distel DL, Dupree P, Etxabe AG, Goodell BS, Jellison J, McGeehan JE, et al. Lignocellulose degradation mechanisms across the tree of life. Curr Opin Chem Biol 2015;29:108–19. https://doi.org/10.1016/j.cbpa.2015.10.018.
[70] Park CH, Kang YK, Im SS. Biodegradability of cellulose fabrics. J Appl Polym Sci 2004;94(1):248–53. https://doi.org/10.1002/app.20879.
[71] Thuaksuban N, Monmaturapoj N, Luntheng T. Effects of polycaprolactone-biphasic calcium phosphate scaffolds on enhancing growth and differentiation of osteoblasts. Bio Med Mater Eng 2018;29(2):159–76. https://doi.org/10.3233/BME-171720.
[72] Tarafder S, Bose S. Polycaprolactone-coated 3D printed tricalcium phosphate scaffolds for bone tissue engineering: in vitro alendronate release behavior and local delivery effect on in vivo osteogenesis. ACS Appl Mater Interfaces 2014;6(13):9955–65. https://doi.org/10.1021/am501048n.
[73] Retegi-Carrión S, Ferrandez-Montero A, Eguiluz A, Ferrari B, Abarrategi A. The effect of $Ca^{2+}$ and $Mg^{2+}$ ions loaded at degradable PLA membranes on the

proliferation and osteoinduction of MSCs. Polymers 2022;14:2422. https://doi.org/10.3390/polym14122422.
[74] Mocanu A, Cadar O, Frangopol PT, Petean I, Tomoaia G, Paltinean GA, Racz CsP, Horovitz O, Tomoaia-Cotisel M. Ion release from hydroxyapatite and substituted hydroxyapatites in different immersion liquids: *in vitro* experiments and theoretical modelling study. R Soc Open Sci 2021;8:201785. https://doi.org/10.1098/rsos.201785.
[75] Otsuka M, Marunaka S, Matsuda Y, Ito A, Layrolle P, Naito H, Ichinose N. Calcium level-responsive in vitro zinc release from zinc-containing tricalcium phosphate (ZnTCP). J Biomed Mater Res 2000;52:810–24. https://doi.org/10.1002/1097-4636(20001215)52:4<819::AID-JBM27>3.0.CO;2-O.
[76] Akobundu UU, Ifijen IH, Duru P, Igboanugo JC, Ekanem I, Fagbolade M, Ajayi AS, George M, Atoe B, Matthews JT. Exploring the role of strontium-based nanoparticles in modulating bone regeneration and antimicrobial resistance: a public health perspective. RSC Adv 2025;15:10902–57. https://doi.org/10.1039/D5RA00308C.
[77] Faria LV, Lopes MES, de Oliveira DP, da Silva FS, Fugivara CS, Nogueira AVB, Deschner J, Cirelli JA. Sustained release of Sr and Ca from a micronanotopographic titanium surface improves osteoblast function. Biometals 2025;38(2):623–46. https://doi.org/10.1007/s10534-025-00668-8.
[78] Fosca M, Streza A, Antoniac IV, Vadalà G, Rau JV. Ion-doped calcium phosphate-based coatings with antibacterial properties. J Funct Biomater 2023;14(5):250. https://doi.org/10.3390/jfb14050250. 29.
[79] Parekh A, Moore M, Janorkar AV, Roach MD. Mg-Doped carbonated hydroxyapatite and tricalcium phosphate anodized coatings on titanium implant alloys. Appl Sci 2024;14:11831. https://doi.org/10.3390/app142411831.
[80] Tuikampee S, Chaijareenont P, Rungsiyakull P, Yavirach A. Titanium surface modification techniques to enhance osteoblasts and bone formation for dental implants: a narrative review on current advances. Metals 2024;14:515. https://doi.org/10.3390/met14050515.
[81] Eliaz N, Metoki N. Calcium phosphate bioceramics: a review of their history, structure, properties, coating technologies and biomedical applications. Materials 2017;10:334. https://doi.org/10.3390/ma10040334.